Journal Homepage: -www.journalijar.com

INTERNATIONAL JOURNAL OF ADVANCED RESEARCH (IJAR)

Article DOI:10.21474/IJAR01/22442
DOI URL: http://dx.doi.org/10.21474/IJAR01/22442

RESEARCH ARTICLE

VARIABILITY OF TOTAL ELECTRON CONTENT (TEC) DURING FOUR MAJOR GEOMAGNETIC STORMS OF 2012–2014: A MULTISITE ANALYSIS AT FIXED LONGITUDES

Moumouni Diallo[1], Saguedo Sawadogo[1],Christian Zoundi[1], Rolland Fleury[2] and Frederic Ouattara[1]

1. Laboratoire De Chimie Analytique, Physique De l'Espace Et De l'Energie (LCAPSE), Universite Norbert ZONGO, Burkina Faso.
2. Lab-STICC, UMR 6285, Institut Mines-Telecom Atlantique, 29288 Brest, Cedex 3, France.

Manuscript Info

Manuscript History
Received: 12 October 2025
Final Accepted: 14 November 2025
Published: December 2025

Key words:
VTEC; geomagnetic storms; PPEF; DDEF; O/N_2 ratio.

Abstract

This study investigates the ionospheric response to four major geomagn etic storms that occurred on 14 July 2012, 17 March 2013, 2 October 2013, and 27 February 2014, focusing on variations in the vertical total electron content (VTEC). VTEC data were obtained from 13 GNSS stations distributed across low, mid, and high-latitude regions along longitudes between 20°E and 40°E. For each event, the mean VTEC of the five geomagnetically quietest days of the corresponding month was used as a reference to characterize storm-time deviations.The results reveal diverse and complex ionospheric responses. The 14 July 2012 storm is characterized by a nighttime VTEC depletion at the equatorial ionization anomaly (EIA) trough, a transient intensification of the EIA, pronounced oscillations, interhemispheric asymmetries, and a subseque nt suppression of the EIA, while high latitudes exhibit persistent depletion. The 17 March 2013 storm shows a pre-storm enhancement of VTEC, followed by oscillatory behavior, a transition from positive to negative storm effects, interhemispheric asymmetries, and EIA suppression. Similarly, the 2 October 2013 storm exhibits an early VTEC enhancement, marked oscillations, high-latitude depletion, and a transition from positive to negative effects at mid-latitudes, with relatively weak responses at low latitudes. In contrast, the 27 February 2014 storm is dominated by a widespread positive VTEC response, except at southern high latitudes where negative effects prevail, together with pronounced interhemispheric asymmetries.

These findings highlight the strong spatiotemporal variability of storm-time ionospheric responses as a function of storm intensity, latitude, and likely the local time of main phase onset. The observed signatures are interpreted in terms of the combined effects of prompt penetration electric fields (PPEF), disturbed dynamo electric fields (DDEF), traveling atmospheric disturbances (TADs), and storm-induced changes in thermospheric composition, particularly variations in the O/N_2 ratio

Introduction:-

The ionosphere, extending from approximately 60 km to 1000 km in altitude, constitutes the ionized component of Earth's upper atmosphere and plays a fundamental role in space weather processes through its coupling with the magnetosphere and its sensitivity to solar and geomagnetic forcing (Pulkkinen 2007; Ouedraogo et al. 2024 ; Alenazi et al. 2025). During geomagnetic storms, the ionosphere undergoes substantial perturbations, commonly referred to as ionospheric storms, which significantly affect radio wave propagation and degrade the accuracy of Global Navigation Satellite System (GNSS) positioning and navigation services (Davies 1990; Blanch et al. 2013; Curto et al. 2018; Atıcı et Sağır 2020). A comprehensive understanding of storm-time ionospheric behavior is therefore crucial for both scientific investigations and operational applications (Migoya-Orue et al. 2009; Liu et al. 2011; Akala et al. 2012).

The ionospheric response to geomagnetic storms depends on multiple factors, including storm intensity, local time, season, geomagnetic latitude and longitude, storm phase, and the prevailing level of solar activity (Prölss 1995; Gao 2008; Mendillo et Narvaez 2009; Pedatella et al. 2009; Mendillo et Narvaez 2010; Vijaya Lekshmi et al. 2011; Immel et Mannucci 2013; Matamba et al. 2015). Based on geomagnetic latitude (GLAT), the ionosphere is commonly classified into low (GLAT < 30°), mid (30° ≤ GLAT < 60°), and high latitudes (GLAT ≥ 60°) (Hunsucker et Hargreaves 2007). Geomagnetic storms are categorized using the Dst index as weak (−50 nT<Dst ≤ −30 nT), moderate (−100 nT<Dst ≤ −50 nT), and intense (Dst ≤ −100 nT) events (Gonzalez et al. 1994).
Among the parameters used to monitor ionospheric disturbances, the vertical total electron content (VTEC) is one of the most sensitive indicators. Storm-time VTEC variability is controlled by several physical mechanisms, including prompt penetration electric fields (PPEF), disturbed dynamo electric fields (DDEF), thermospheric composition changes, and storm-induced neutral winds. The interplay of these processes can lead to either positive or negative ionospheric storm effects, depending on geophysical conditions (Prölss 1995; Buonsanto 1999; Richmond et Lu 2000; Mendillo 2006; Balan et al. 2010).

Numerous studies have examined TEC variability during major geomagnetic storms of solar cycle 24, particularly between 2012 and 2014. However, most investigations have focused on the American and Asian longitude sectors (Qian, Solomon, et al. 2014; Chakraborty et al. 2015; Mao et al. 2015; Shreedevi et Choudhary 2017; Migoya-Orue et al. 2021; Zhu et al. 2022). In contrast, studies in the Europe–Africa sector remain relatively sparse and fragmented. Akala et al. (2013) investigated equatorial and mid-latitude responses in East Africa, while Azzouzi (2016) analyzed storm-time ionospheric behavior at mid and high latitudes over the Europe–Africa region. More localized studies using a limited number of GNSS stations were conducted by Malki et al. (2018) and Habyarimana (2023). Tesema et al. (2015), although covering a relatively broad latitudinal range, did not include southern high latitudes and focused primarily on VTEC map-based interpretations. Shimeis et al. (2015) analyzed TEC variations along a latitudinal chain of GPS stations between 20°E and 40°E, spanning from northern to southern high latitudes, but their study was limited to the 5 April 2010 storm. Global modeling and simulation studies (Yue et al. 2016) have included the Europe–Africa sector; however, their emphasis remained predominantly on the American and Asian sectors. Despite providing valuable insights into the underlying physical mechanisms (PPEF, DDEF, neutral winds, and thermospheric composition changes expressed through the O/N_2 ratio), these studies do not offer a comprehensive and coherent regional analysis covering all latitudes along a fixed longitude sector.

In this context, the present study aims to analyze VTEC variability during four major geomagnetic storms of solar cycle 24 using GNSS stations distributed along a Europe–Africa–Antarctic meridional chain between 20°E and 40°E. The methodology combines a station-by-station analysis, in which daily VTEC variations are compared with the mean VTEC of the five quietest days of the corresponding month, with the analysis of regional VTEC and ΔVTEC maps. This approach allows for a detailed characterization of both local and regional ionospheric responses and provides new insight into the equatorial and interhemispheric dynamics associated with geomagnetic storms.
The paper is organized as follows: Section 2 describes the data and methodology, Section 3 presents and discusses the results, and Section 4 provides the interpretation and main conclusions.

Data and Methods:-

Data

Solar Wind and Geomagnetic Parameters

In this study, we used several solar wind parameters, including the solar wind speed (Vsw, km s^{-1}), solar wind dynamic pressure (Psw, nPa), and the south–north component of the interplanetary magnetic field (IMF Bz, nT), as

well as geomagnetic indices such as the auroral electrojet index (AE, nT), the symmetric ring current index (SYM/H, nT), the equatorial Dst index, and the planetary Kp index.

Time series of Vsw, Psw, Bz, AE, and SYM/H were obtained from the OMNI database with a 1-minute temporal resolution, available at the OMNIWeb portal (https://omniweb.gsfc.nasa.gov/form/omni_min.html). The Kp and Dst indices, together with the storm sudden commencement (SSC) times marking the abrupt onset of geomagnetic storms, were retrieved from the International Service of Geomagnetic Indices (ISGI) website (https://isgi.unistra.fr/data_download.php).

The SYM/H index, which is closely related to the Dst index, provides a higher temporal resolution and allows for a more detailed monitoring of ring current evolution and associated variations in Earth's magnetic field. All these parameters were used to identify isolated geomagnetic storms, quantify their intensity, and track their temporal evolution (Gonzalez et al. 1994; Tsurutani et al. 1997; Kelley 2009).

Ionospheric Parameter: VTEC

The ionospheric response to the geomagnetic storms of 14 July 2012, 17 March 2013, 2 October 2013, and 27 February 2014 was analyzed using vertical total electron content (VTEC) data computed with software developed by Fleury (MATLAB-based code, www.girgea.org). The analysis is based on observations from 13 GNSS stations regularly distributed across low-, mid-, and high-latitude regions along a longitudinal sector between 20°E and 40°E. RINEX observation files for the selected stations were downloaded from the UNAVCO data archive (http://www.unavco.org). Figure 1 shows the geographical distribution of the GNSS stations used in this study, together with the position of the magnetic equator, located near 10° N in geographic latitude. The magnetic equator is an essential reference, as the equatorial ionization anomaly (EIA) is strongly controlled by the geomagnetic field configuration. Table 1 lists the geographic and geomagnetic coordinates of all stations.

The ionospheric parameter considered in this study is the vertical total electron content (VTEC), which represents the number of electrons contained in a vertical column of 1 m² cross-sectional area extending up to the satellite altitude. The slant total electron content (STEC) was computed using the dual-frequency combination (f_1 = 1575.42 MHz and f_2 = 1227.60 MHz) of pseudorange measurements contained in the RINEX files, with a temporal resolution of 30 s.

STEC values were calibrated by accounting for satellite differential code biases (DCBs) provided by the Center for Orbit Determination in Europe (CODE) at the University of Bern. Receiver DCBs were estimated by fitting the measured STEC to STEC values derived from the GIM/CODG model (ftp.aiub.unibe.ch). The DCB applied corresponds to the daily mean value. A mapping function with a reference height of 450 km was then used to convert STEC to VTEC (Ouedraogo et al. 2024; Ouattara et al. 2011):

$$\mathrm{VTEC} = \mathrm{STEC} \times \sqrt{1 - \left(\frac{R_T \cos e}{R_T + h_{\mathrm{ref}}}\right)^2}$$

where R_T is Earth's radius, e is the satellite elevation angle, and h_{ref} denotes the reference height.

VTEC is expressed in total electron content units (TECU), where 1 TECU = 10^{16} electrons. m^{-2}. VTEC values are assigned to the ionospheric pierce point (IPP) corresponding to each satellite. The vertical TEC above each station was finally obtained through an inverse-square elevation-weighted regression applied to all satellite observations within each time interval. The use of VTEC is particularly relevant, as it provides a direct indicator of the global ionospheric state and enables an accurate characterization of ionospheric variability during geomagnetic storms.

Thermospheric Composition Data:-

In addition, global maps of the [O/N_2] ratio derived from the Global Ultraviolet Imager (GUVI) onboard the TIMED satellite were used to support the interpretation of the results. These maps, available from the portal https://guvitimed.jhuapl.edu/guvi-galleryl3on2_new/, constitute a key indicator of the thermospheric state and of electron density variations in the ionospheric F region (Yu et al. 2023).

A decrease in atomic oxygen reduces ion production, while an increase in molecular nitrogen enhances ion loss through recombination processes, leading to a net decrease in electron density (Prölss 1995). Consequently, the [O/N_2] ratio is particularly well suited for assessing ionospheric and thermospheric responses to geomagnetic storms (Rishbeth et Müller-Wodarg 2006; Fuller-Rowell et al. 2007; Yue et al. 2014).

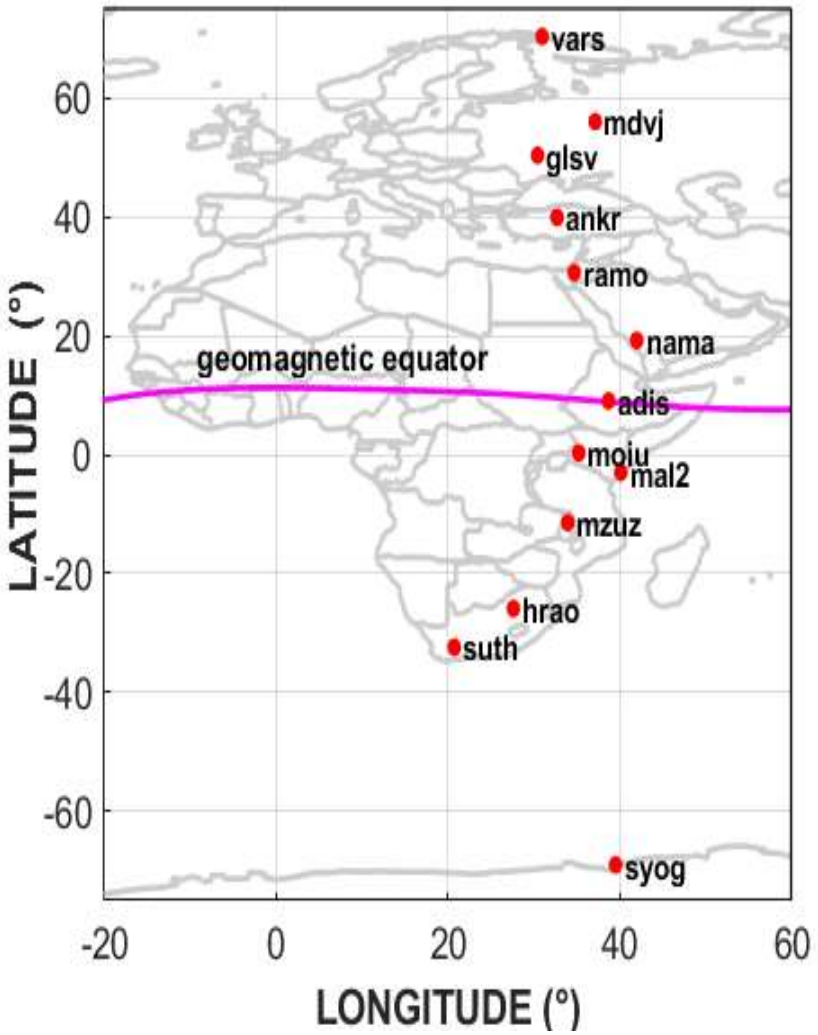

Figure 1: Map showing the location of the selected GNSS receivers

Table 1: GNSS stations and their geographic and geomagnetic coordinates.

Region	Station	Lat (°)	Lon (°)	Lat mag. (°)	Lon mag. (°)	Local Time
High latitude	VARS	70.33	31.03	66.50	113.32	UTC+2h
Mid-latitude	SVTL	60.53	29.78	56.61	106.79	UTC+2h
	GLSV	50.36	30.50	45.96	104.50	UTC+2h
	ANKR	39.89	32.76	34.24	04.97	UTC+2h
Low latitude	RAMO	30.60	34.76	23.36	106.26	UTC+2h
	NAMA	19.21	42.04	11.49	113.60	UTC+3h
	ADIS	9.03	38.76	0.16	110.46	UTC+3h
	MOIU	0.29	35.29	-9.17	107.00	UTC+2h
	MAL2	-3.0	40.19	-12.43	111.86	UTC+3h
	MZUZ	-11.42	34.01	-21.87	104.92	UTC+2h
Mid-latitude	HRAO	-25.89	27.69	-36.32	94.69	UTC+2h
	SUTH	-32.38	20.81	-41.09	84.76	UTC+1h
High latitude	SYOG	-69.00	39.58	-66.08	71.65	UTC+3h

Method:-

This study focuses on the analysis of the ionospheric response to geomagnetic storms with sudden commencements (SSC) that occurred during the maximum phase of solar cycle 24 (2012–2014). Event selection was based on two main criteria.

(1) Storm isolation: only geomagnetic storms with a planetary Kp index ≥ 5 and a minimum Dst index ≤ −50 nT were considered. In addition, magnetically quiet conditions before and after the SSC were required to ensure that the selected storms were isolated events, following the methodology adopted by Azzouzi (2016) and Bazie et al. (2025); (2) Availability of GNSS data: the selection was restricted to events for which ionospheric data were available at all or most of the GNSS stations considered, thereby ensuring sufficient spatial and temporal coverage for a reliable analysis.

As a reference, we adopted the mean VTEC computed from the five geomagnetically quietest days of the month corresponding to each storm (Chakraborty et al. 2015; Kuai et al. 2016; Omojola et Adewumi 2019; Sharma et al. 2020; Berenyi et al. 2023; Sawadogo et al. 2023; Silwal et al. 2023; Uga et al. 2024). The list of these quiet days is available at https://datapub.gfz.de/download/10.5880.Kp.0001/Quiet_Disturbed_Days/.

Two complementary approaches were employed. The qualitative analysis consists of a direct comparison between storm-time VTEC temporal variations and the mean VTEC of the quiet days, allowing a visual assessment of ionospheric disturbances (positive, negative, or negligible deviations). The quantitative analysis is based on the relative VTEC deviation (ΔVTEC, %), expressed as a percentage, in order to accurately quantify the magnitude of the ionospheric perturbations. This deviation is defined as :

$$\Delta\mathrm{VTEC}(\%) = \frac{\mathrm{VTEC}_S - \mathrm{VTEC}_Q}{\mathrm{VTEC}_Q} \times 100$$

where VTEC_S denotes the daily mean VTEC during storm conditions, and VTEC_Q represents the daily mean VTEC averaged over the five quietest days of the corresponding month.

Table 2 summarizes the geomagnetic storms selected for this study, providing the SSC dates, minimum Dst values ($\mathrm{Dst}_{\min}$), maximum Kp indices ($\mathrm{Kp}_{\max}$), the corresponding season, and the five quietest days of the month.The season during which each storm occurred is specified in order to explain the interhemispheric asymmetry of VTEC. Indeed, the intensity and dominant direction of neutral winds vary with the seasons, leading to significant differences between hemispheres and promoting stronger plasma anomalies in winter than in summer (Astafyeva 2009).Therefore, to analyze storm effects as a function of season, the seasons were classified following the method proposed by (Azzouzi 2016). Accordingly, storm events were binned into seasonal categories following this classification scheme: March–April equinox, September–October equinox, summer solstice (May–August), and winter solstice (November–February)

Table 2: Extreme Dst and Kp values during the selected geomagnetic storms and the quiet days of the corresponding months.

N°	Date of storm	SCC time	Kp (max)	Dst (min)	Season	The five quietest days of the month in order
1	14/07/2012	18 :09 :00	7	-139	Solstice	13 ;26 ;27 ;18 et 31
2	17/03/2013	05 :59 :48	7	-132	Equinoxe	08 ;07 ;26 ;25 et 13
3	02/10/2013	01 :54 :36	8	-72	Equinoxe	05 ;28 ;04 ;19 et 21
4	27/02/2014	16 :50 :00	5	-97	Solstice	13 ;26 ;14 ;25 et 02

Results:-

Evolution of Interplanetary Parameters and Geomagnetic Indices during the Storms

Figures 2a–2d show the temporal variations of the solar wind speed (Vsw, km s^{-1}), solar wind dynamic pressure (Psw, nPa), the south–north component of the interplanetary magnetic field (IMF Bz, nT), the auroral electrojet index (AE, nT), and the symmetric ring current index (SYM/H, nT), with a 1-min temporal resolution, for the periods 13–18 July 2012, 15–20 March 2013, 30 September–5 October 2013, and 26 February–3 March 2014, respectively. In each figure, the vertical magenta line and the shaded area indicate the storm sudden commencement (SSC) and the main phase of the geomagnetic storm, respectively.

We first analyze the period from 13 to 18 July 2012 (Figure 2a). After a magnetically quiet interval, the arrival of the interplanetary shock (SSC) at 18:09 UT was followed by a rapid increase in solar wind speed, reaching 681.9 km s^{-1}, accompanied by strong magnetospheric compression as indicated by a peak dynamic pressure of 28.46 nPa. The IMF Bz component, initially weak and southward oriented, exhibited oscillations between −20 and +22 nT until about 06:42 UT on 15 July, before remaining persistently southward for nearly 32 hours (until approximately 15:00 UT on 16 July). This prolonged southward orientation favored efficient coupling between the solar wind magnetic field and the terrestrial magnetosphere.

Auroral activity intensified markedly, with the AE index reaching a maximum value of 1772 nT at 18:48 UT on 14 July. The SYM/H index showed an initial positive excursion up to +51 nT, followed by a sharp decrease to −123 nT at 10:04 UT on 15 July, marking the end of the storm main phase. This was followed by a gradual recovery phase, which concluded around 10:00 UT on 18 July.

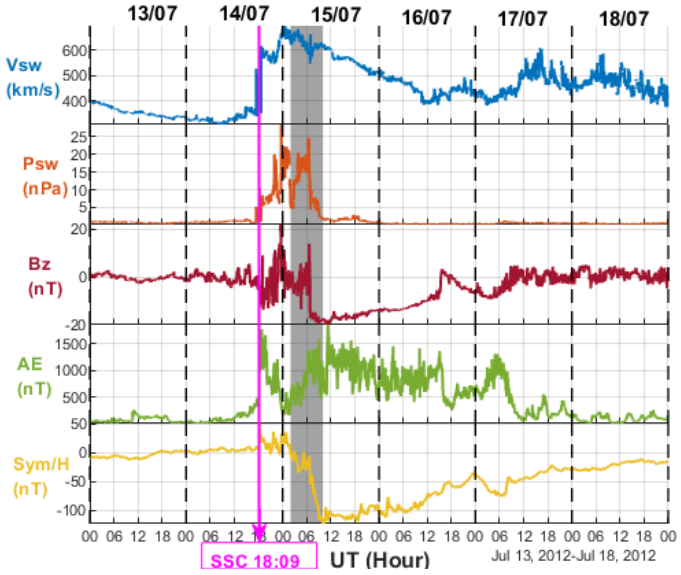

Figure 2.a: From top to bottom, it illustrates the temporal variations of Vsw (km/s), Psw (nPa), Bz (nT), AE (nT), and SYM/H (nT) with a resolution of one minute for the period from July 13 to 18, 2012.

On 15 March 2013, at around 06:00 UT, NASA reported the eruption of a magnetic filament near the sunspot region AR1692. This eruption produced an M1-class solar flare and a coronal mass ejection (CME) directed toward Earth with an estimated speed of about 900 km s^{-1} (Habyarimana 2023). The CME reached Earth at approximately 06:00 UT on 17 March 2013, triggering an intense geomagnetic storm commonly referred to as the "St. Patrick's Day storm" (Yue et al. 2016).

Solar wind conditions and geomagnetic activity from 15 to 20 March 2013 are shown in Figure 2b. As illustrated in the figure, immediately after the arrival of the solar wind shock, marked by an SSC at 06:00 UT on 17 March 2013, the solar wind speed increased rapidly, reaching 757.4 km s^{-1} at 10:38 UT, while the dynamic pressure peaked at 24.18 nPa at 07:41 UT and remained above 5 nPa for more than 11 hours. During this interval, the IMF Bz component oscillated between −19.34 and +12.22 nT before turning persistently southward around 15:00 UT.
Auroral activity intensified significantly, with the AE index reaching a maximum value of approximately 2689 nT at 16:51 UT, indicating strong auroral current activity. The SYM/H index exhibited an initial positive excursion followed by a sharp decrease to −132 nT at 20:28 UT on 17 March 2013, marking the end of the storm main phase, after which a gradual recovery phase extended until 20 March.

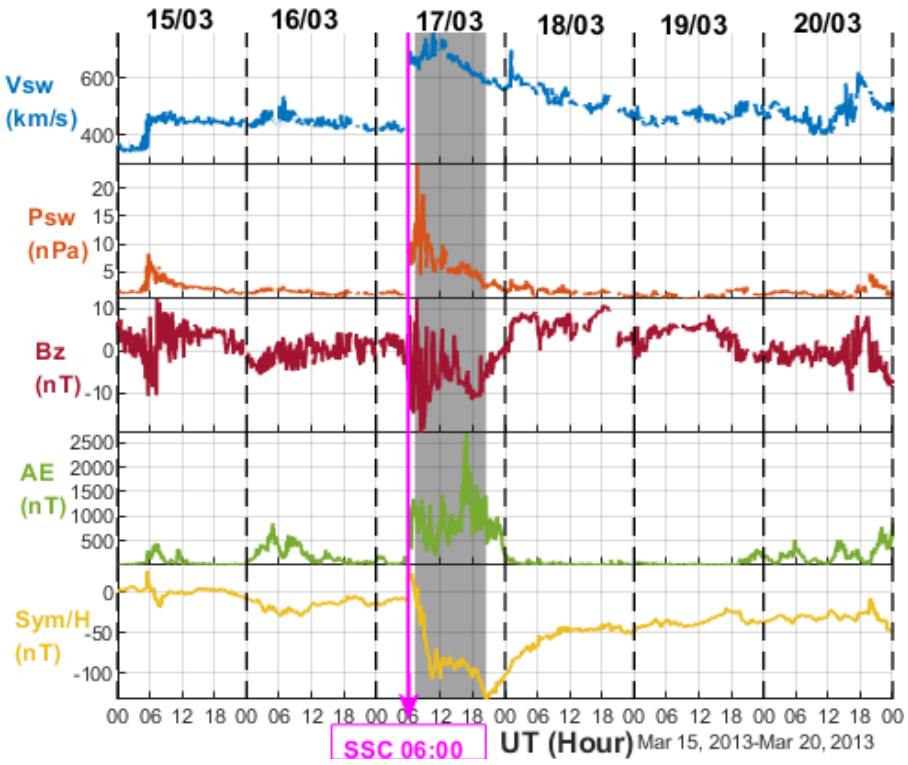

Figure 2.b shows, from top to bottom, the temporal variations of Vsw (km/s), Psw (nPa), Bz (nT), AE (nT), and SYM/H (nT) with a resolution of one minute for the period from March 15 to 20, 2013.

The panels of Figure 2c (from top to bottom) illustrate the evolution of solar wind and geomagnetic parameters from 30 September to 5 October 2013. On 2 October, immediately after the SSC, the solar wind speed abruptly increased from 363.4 km s^{-1} to more than 644 km s^{-1} at 04:15 UT, while the solar wind dynamic pressure (Psw) rose from 1.62 nPa to a maximum value of 53.17 nPa at 05:25 UT, indicating the arrival of a solar particle cloud. During this interval, the IMF Bz component exhibited strong fluctuations between 02:00 and 05:00 UT before turning northward and returning to near-normal levels.

The AE index showed a sharp increase, reaching a first peak of 2089 nT at 02:59 UT, then decreasing below 300 nT around 04:30 UT, before displaying a second peak of 1941 nT at 06:00 UT. Later, AE increased again to 1259 nT around 20:30 UT before returning to quiet values toward the end of the storm. The SYM/H index initially increased to 62 nT at 01:58 UT, then dropped to a minimum of −90 nT at 06:19 UT, with a brief positive excursion around 04:30 UT, followed by a gradual recovery.

The geomagnetic storm of 27 February 2014

was most likely caused by a coronal mass ejection (CME) associated with the solar eruption of 25 February 2014. Solar wind conditions and geomagnetic activity from 26 February to 3 March 2014 are shown in Figure 2d. Immediately after the SSC at 16:50 UT on 27 February, the solar wind speed increased from 350 km s^{-1} to 482.8 km s^{-1} at 20:16 UT, while the dynamic pressure reached 17.02 nPa at 17:11 UT.

The IMF Bz component fluctuated between −18 and +12 nT, remaining predominantly southward until about 02:00 UT on 28 February. During this period, the AE index reached a maximum value of 1171 nT at 18:54 UT before returning to near-quiet levels around 05:00 UT on 28 February, with sporadic enhancements persisting until 3 March. The SYM/H index initially increased to +19 nT and then dropped to −101 nT at 23:24 UT, marking the end of the storm main phase, followed by a gradual recovery with minor fluctuations until quiet conditions were restored on 3 March.

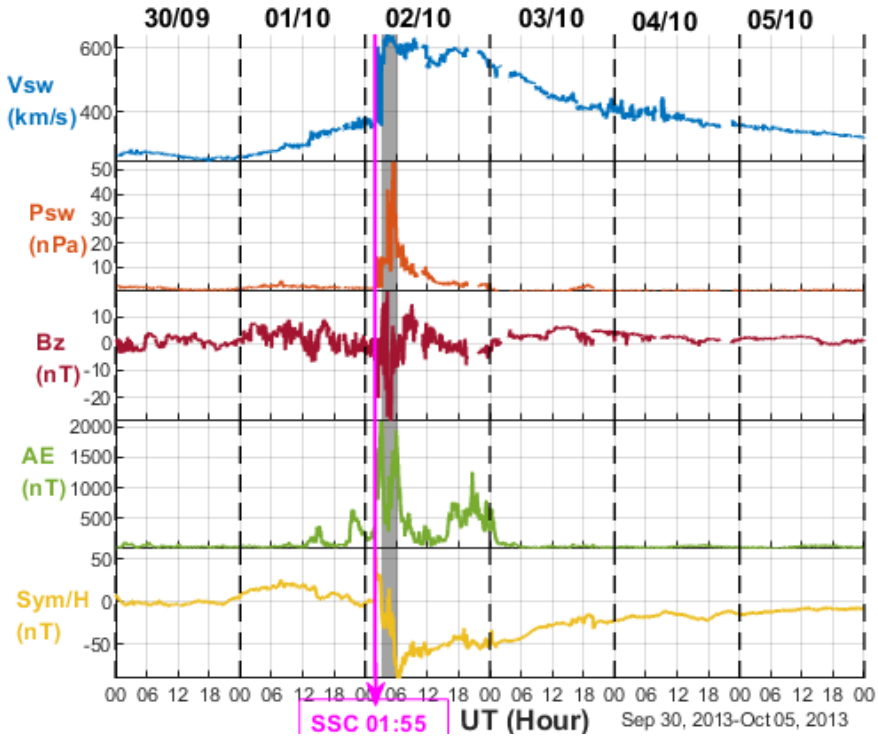

Figure 2c: From top to bottom, temporal variations of Vsw (km s^{-1}), Psw (nPa), Bz (nT), AE (nT), and SYM/H (nT) at a 1-minute resolution for the period 30 September–5 October 2013.

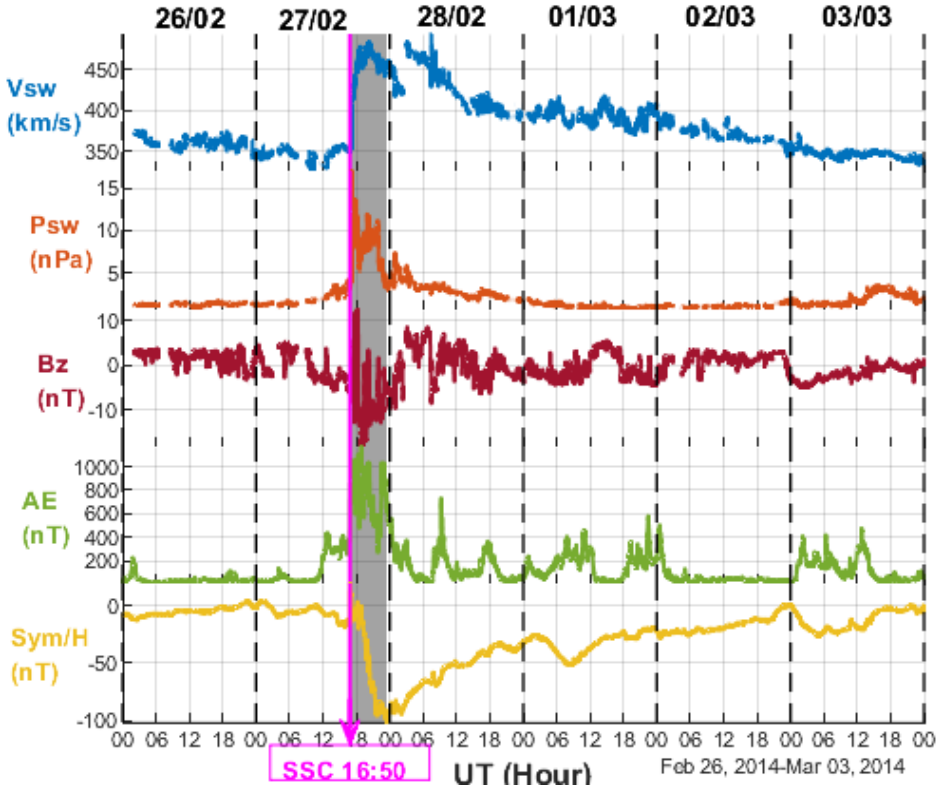

Figure 2d: From top to bottom, temporal variations of Vsw (km s^{-1}), Psw (nPa), Bz (nT), AE (nT), and SYM/H (nT) at a 1-minute resolution for the period 26 February–3 March 2014.

VTEC Response to Geomagnetic Storms

To analyze the ionospheric response to geomagnetic storms, three complementary representations were used. Station-by-station VTEC time series highlight local variability by comparing disturbed conditions with quiet-day levels expressed in TECU. Spatio-temporal VTEC maps provide a regional view of ionospheric dynamics and storm-time responses. The relative deviation ΔVTEC is computed as the difference between daily VTEC values and the mean VTEC of the five quietest days of the corresponding month. These regional VTEC and ΔVTEC maps were generated using MATLAB-based graphical routines.

In the station-by-station overlays, stations are ordered from top to bottom according to decreasing latitude from north to south. The red curve represents storm-time VTEC, the blue curve corresponds to the mean VTEC of the five quiet days, and the light-blue shaded band indicates a ±20% variability range around the quiet-day mean. The vertically shaded gray areas delimit the storm main phase. The spatio-temporal maps display absolute VTEC values and relative deviations ΔVTEC as a function of universal time, for latitudes between −75° and 75° and longitudes between 20°E and 40°E. The vertical magenta line marks the SSC onset time in each figure.

The 14 July 2012 Storm

Figures 3a–3c respectively show the VTEC variations, the spatio-temporal VTEC maps, and the relative deviation ΔVTEC (%) for the period 13–18 July 2012.

In Figure 3a, between 13 and 14 July, prior to storm onset, all stations—except RAMO and ANKR, located near the boundary between low and mid-northern latitudes, which exhibited a slight increase just before storm onset—display a typical diurnal VTEC cycle: a gradual morning increase, a local midday maximum that is more pronounced at low latitudes (e.g., 44.62 TECU at ADIS on 13 July) than at high latitudes (9.58 TECU at SYOG), followed by an evening decrease to nocturnal minima. During this period, VTEC curves remain within the error band around the reference, confirming the absence of significant ionospheric disturbances prior to storm onset.

After the SSC, no clear anomaly is observed until around 23 UT on 14 July. At that time, stations near the equatorial ionization anomaly (EIA) trough, such as NAMA, ADIS, and MOIU, record a slight VTEC depletion, while stations located near the EIA crests (RAMO, MZUZ) show a moderate enhancement.

On 15 July, maximum VTEC values increased significantly compared to the quiet reference and the pre-storm days, except at ADIS, located near the equatorial trough, where the maximum value (48.6 TECU) remained comparable to the reference (48.8 TECU). The VTEC enhancement is particularly pronounced in the Southern Hemisphere. For instance, SUTH recorded a maximum of 37.7 TECU on 15 July, compared to 19.2 TECU for the quiet reference, corresponding to an increase of 18.5 TECU, and 17.3 TECU on 14 July, representing a 20.4 TECU increase relative to the previous day. In contrast, ADIS and MOIU exhibit a simultaneous trough when maxima are recorded elsewhere.

During the night of 15–16 July, before 00 UT, low-latitude stations in the Northern Hemisphere register a decrease in VTEC, while those in the Southern Hemisphere show an increase. At 00 UT, all stations reach minimum values, with a particularly strong decrease at ADIS, located within the anomaly trough. Between 16 and 18 July, high-latitude stations in both hemispheres display VTEC values lower than the quiet reference, followed by a gradual recovery on 18 July. At mid- and low latitudes, an interhemispheric asymmetry is evident: in the Northern Hemisphere, only weak VTEC fluctuations persist until 18 July, whereas in the Southern Hemisphere, more pronounced enhancements appear on 16 July before a gradual recovery. For example, at ANKR, the maximum VTEC on 16 July reaches 27.5 TECU compared to 25.3 TECU for the reference (+2.2 TECU), while at MAL2 the maximum reaches 54.7 TECU compared to 33.9 TECU for the reference, corresponding to an increase of 20.8 TECU.

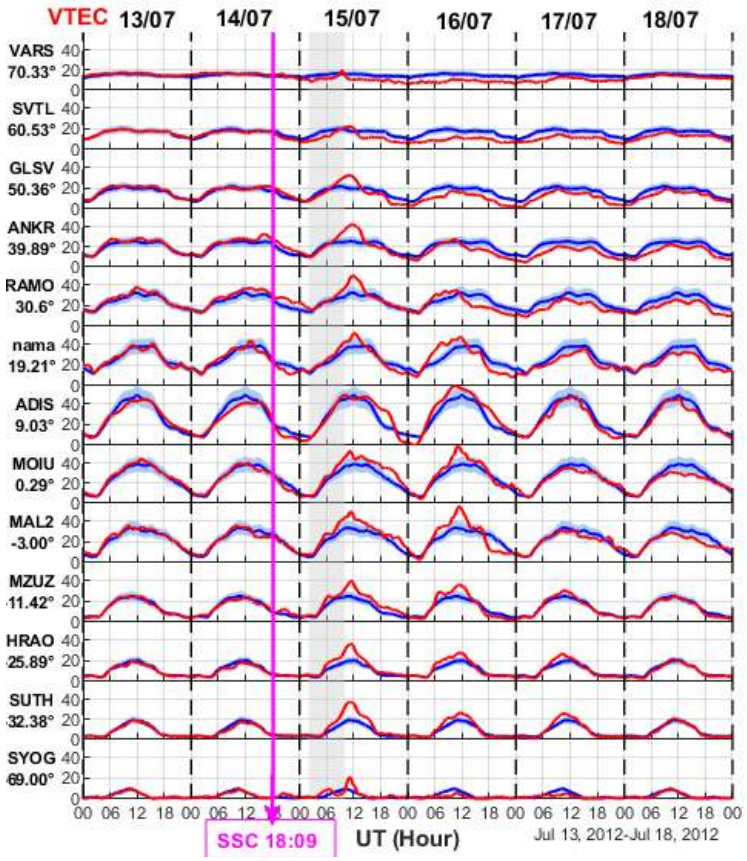

Figure 3a:Temporal variation of vertical total electron content (VTEC) observed at multiple GNSS stations from 13 to 18 July 2012. The vertical magenta line marks the Sudden Storm Commencement (SSC) at 18:09 UT, highlighting the ionospheric response to the geomagnetic disturbance across different latitudes.

Figure 3b highlights a marked intensification of the equatorial ionization anomaly (EIA) on 15 July, characterized by two crests extending toward higher latitudes. On 16 July, VTEC values around the magnetic equator increase significantly compared to 15 July, accompanied by a weakening of the EIA structure. From 17 to 18 July, maximum VTEC values gradually recenter around the magnetic equator and decrease in intensity until 18 July.

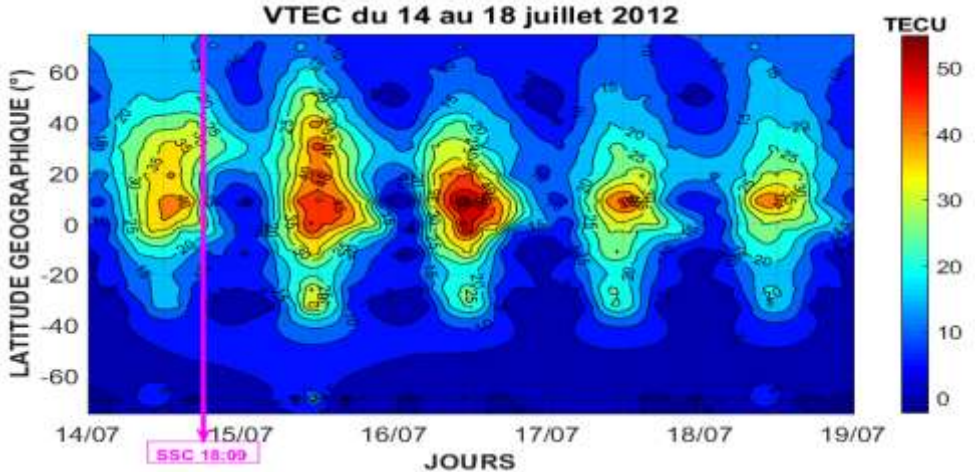

Figure 3b:Latitude–time contour map of vertical total electron content (VTEC) from 14 to 18 July 2012. The color scale (in TECU) illustrates the latitudinal distribution and temporal evolution of ionospheric electron content, with the magenta line indicating the SSC at 18:09 UT.

Figure 3c reveals several significant ΔVTEC enhancements, particularly around 10°S latitude near 19 UT on 14 and 15 July, reaching about 40% and 80%, respectively, as well as at mid-latitudes in both hemispheres around local noon on 15 July, with increases of approximately 40%. The figure also shows pronounced ΔVTEC decreases (negative ionospheric storm phase) in the equatorial region around 01 UT on 15 and 16 July, reaching −40% and −80%, respectively, and at high latitudes in both hemispheres, where reductions range between −40% and −60%.

During the storm, ΔVTEC enhancements are more pronounced in the Southern Hemisphere than in the Northern Hemisphere, while depletions are stronger in the Northern Hemisphere. This behavior is consistent with the seasonal context of the storm, which occurred near the solstice, corresponding to summer in the Northern Hemisphere and winter in the Southern Hemisphere.

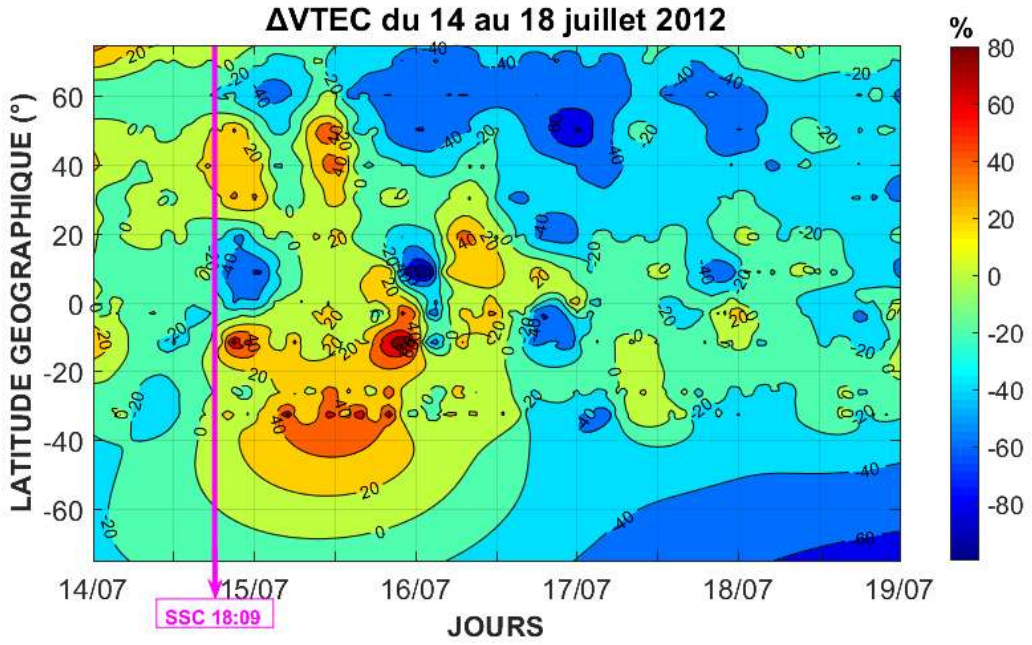

Figure 3c:Latitude–time contour map of relative variations in vertical total electron content (ΔVTEC, %) from 14 to 18 July 2012. The color scale represents percentage deviations from quiet-time conditions. The magenta line marks SSC at 18:09 UT.

The 17 March 2013 Storm

Figures 4a–4c respectively illustrate the VTEC variations, the spatiotemporal VTEC maps, and the relative deviation ΔVTEC (%) for the period from 15 to 20 March 2013.

Figure 4a shows the VTEC variations between 15 and 20 March 2013. On 16 March, the day preceding the storm and considered geomagnetically quiet, the maximum VTEC values at all stations are higher than the reference values, with increases ranging from +1.4 TECU at SYOG (25.7 TECU compared to 24.3 TECU for the reference) to +20.2 TECU at NAMA (82.4 TECU compared to 62.2 TECU for the reference).

On 17 March, during the storm main phase, all stations record maximum VTEC values higher than the reference, except for SYOG (southern high latitude). The most pronounced increases are observed at northern high latitudes and at northern and southern mid-latitudes, as well as at stations located near the magnetic equator (ADIS, MOIU), with enhancements ranging from +13.6 TECU (MOIU) to +28.6 TECU (ANKR) relative to the reference, and from +5.5 TECU (MOIU) to +20.7 TECU (GLSV) relative to 16 March. In contrast, stations located near the crests of the equatorial ionization anomaly (EIA) (NAMA, MAL2, MZUZ) show weak increases relative to the reference and slight decreases compared to 16 March, indicating an inhibition of the EIA.

During the recovery phase, 18 March is characterized by contrasting responses: most stations exhibit weak VTEC fluctuations, whereas ADIS and SYOG show, respectively, a strong increase and a pronounced decrease (ADIS: 79.1 TECU versus 61.8 TECU for the reference, i.e., +17.3 TECU; SYOG: 14.5 TECU versus 24.3 TECU, i.e., −9.8 TECU). On 19 March, stations located near the EIA crests record increases exceeding +10 TECU relative to the reference, notably RAMO (+10.4 TECU), NAMA (+18.5 TECU), and MZUZ (+12.0 TECU), reflecting a

strengthening of the EIA. Finally, on 20 March, all stations return to values comparable to quiet conditions, indicating a recovery of the ionosphere, except at ADIS where an increase of +11.2 TECU is still observed.

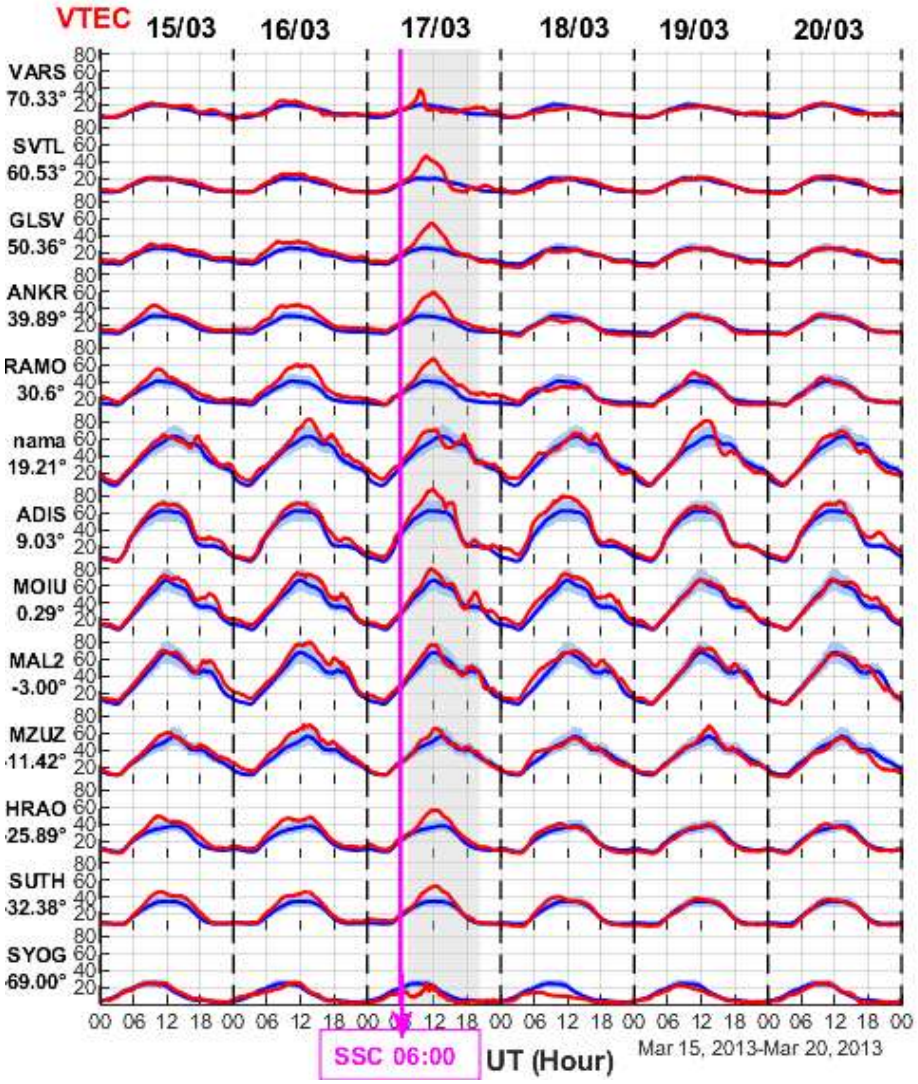

Figure 4a: Temporal variation of vertical total electron content (VTEC) observed at multiple GNSS stations from 15 to 20 March 2013. The vertical magenta line marks the SSC at 06:00 UT, highlighting the ionospheric response to the geomagnetic disturbance across different latitudes.

Figure 4b shows that on 16 March, the day preceding the storm, two well-defined crests of the equatorial ionization anomaly (EIA) are clearly visible. In contrast, on 17 March, the storm day, these crests disappear, accompanied by an increase in VTEC around the magnetic equator, at northern and southern mid-latitudes—more pronounced in the Northern Hemisphere—and at northern high latitudes. On 18 March, the crests remain absent, and a decrease in VTEC is observed at all latitudes compared to 17 March, with a particularly strong reduction at northern mid-latitudes. On 19 March, the EIA crests reappear, with the northern crest being more developed than the southern one. Finally, on 20 March, the crests disappear again, while an increase in VTEC is observed around the magnetic equator.

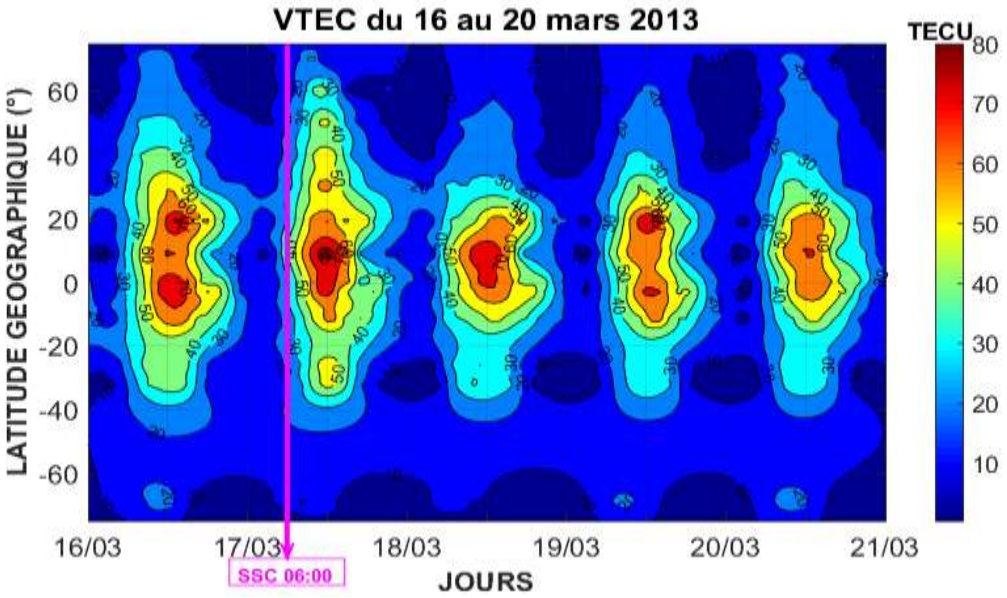

Figure 4b: Latitude–time contour map of vertical total electron content (VTEC) from 16 to 20 March 2013. The color scale (in TECU) illustrates the latitudinal distribution and temporal evolution of ionospheric electron content, with the magenta line indicating the SSC at 06:00 UT.

Figure 4c highlights several significant increases (ΔVTEC > +50%) around 01 UT, located at the EIA crests and at northern mid-latitudes, around 04 UT and 14 UT on 16 March, the day preceding the storm. On 17 March, the storm day, a marked positive ionospheric storm appears around 01 UT, prior to the storm onset at 06 UT, with ΔVTEC values exceeding +100% near the magnetic equator. During the main phase, substantial VTEC enhancements are also observed around 12 UT at northern mid-latitudes. After 12 UT, the positive ionospheric storm progressively extends from northern mid-latitudes toward low latitudes, reaching the magnetic equator around 22 UT, where the positive effect intensifies strongly around 01 UT on 18 March, with ΔVTEC values reaching up to +200%. Around 22 UT on 17 March, an increase is also observed at northern high latitudes. Finally, on 19 and 20 March, strong positive deviations (ΔVTEC > +50%) persist only near the magnetic equator around 01 UT each day, while negative deviations appear at southern high latitudes on 18 March around 10 UT.

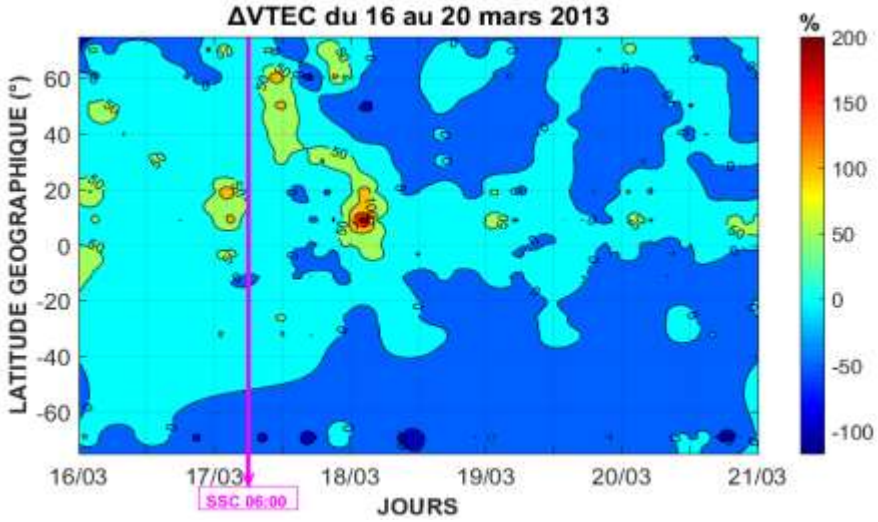

Figure 4c: Latitude–time contour map of relative variations in vertical total electron content (ΔVTEC, %) from 16 to 20 March 2013. The color scale represents percentage deviations from quiet-time conditions. The magenta line marks the SSC at 06:00 UT.

3.2.3 The 02 October 2013 Storm

Figure 5a presents the VTEC variations from 30 September to 5 October 2013. On 1 October, a geomagnetically quiet day, the maximum VTEC values recorded at all stations decreased relative to the reference, with differences ranging from −1.8 TECU to −14.7 TECU (SVTL: −1.8 TECU; MZUZ: −14.7 TECU), except for the VARS station, whose maximum value (21.9 TECU) remains comparable to the reference (21.3 TECU).

On 2 October, the storm day, stations located at northern and southern mid-latitudes exhibit a clear increase in maximum VTEC values relative to the quiet reference and to the days preceding the storm, with peaks occurring mainly between 06 UT and 12 UT. These increases are more pronounced in the Northern Hemisphere, particularly at ANKR (+16.0 TECU) and RAMO (+13.9 TECU), compared to +7.7 TECU at HRAO and +3.2 TECU at SUTH in the Southern Hemisphere. Low-latitude stations do not show notable variations but display oscillatory VTEC behavior. In contrast, at northern and southern high latitudes, a decrease in maximum VTEC values relative to the reference is observed, particularly at SYOG (−13.3 TECU) and, to a lesser extent, at VARS (−4.2 TECU). During the evening of 2 October, between 18 UT and 00 UT, a slight increase in VTEC is observed in the Northern Hemisphere. From 3 to 5 October, the maximum VTEC values decrease each day relative to the quiet reference, with more pronounced reductions at high and mid-latitudes in both hemispheres.

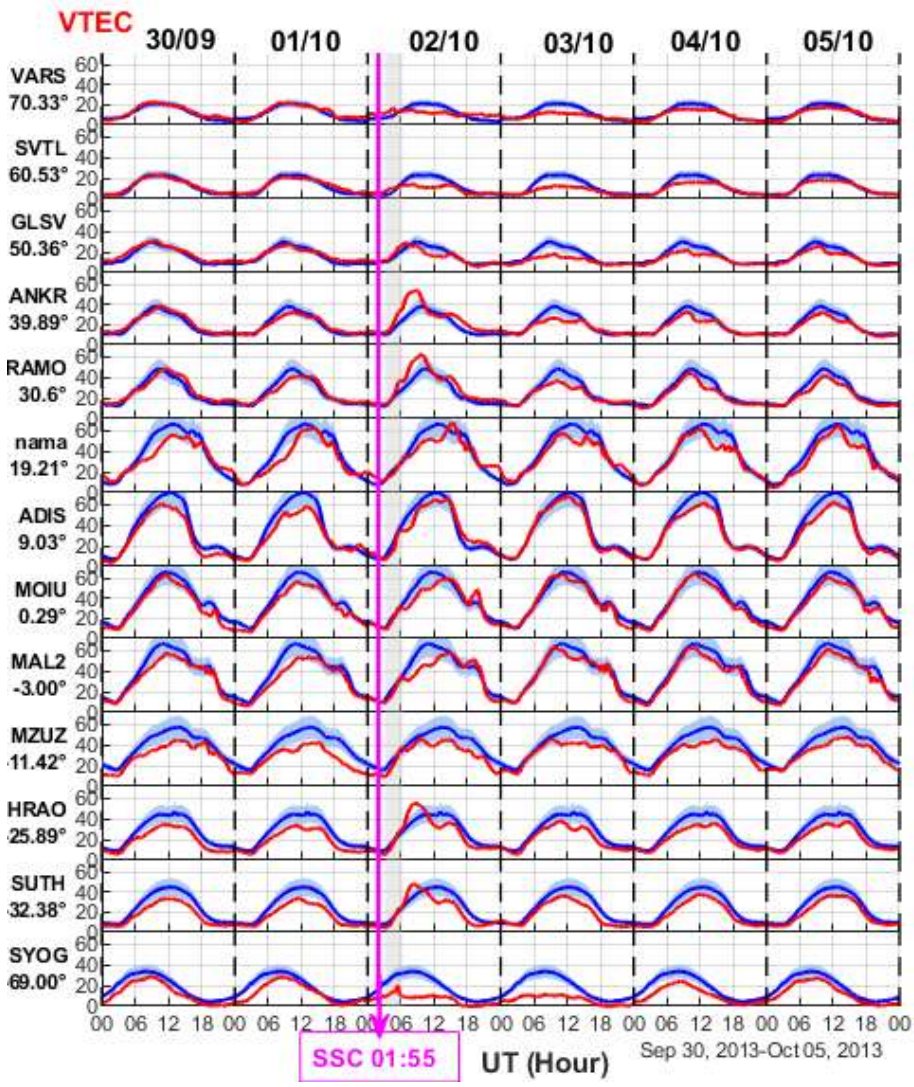

Figure 5a: Temporal variation of vertical total electron content (VTEC) observed at multiple GNSS stations from 30 September to 05 October 2013. The vertical magenta line marks the SSC at 01:55 UT, highlighting the ionospheric response to the geomagnetic disturbance across different latitudes.

Figure 5b illustrates that on the quiet day preceding the geomagnetic storm (1 October), a VTEC peak of about 60 TECU is located at the northern crest of the equatorial ionization anomaly (EIA). On 2 October, the storm day, a strong increase in VTEC (approximately 50 TECU) is observed at northern and southern mid-latitudes as well as at the magnetic equator (about 60 TECU), with peaks first occurring at mid-latitudes and subsequently at the equator. On 3 October, the VTEC intensifies around the magnetic equator, forming a broadened band, while the EIA crests are inhibited. On 4 and 5 October, peaks reappear both in the trough region and at the EIA crests, accompanied by a slight northward expansion of the enhanced VTEC.

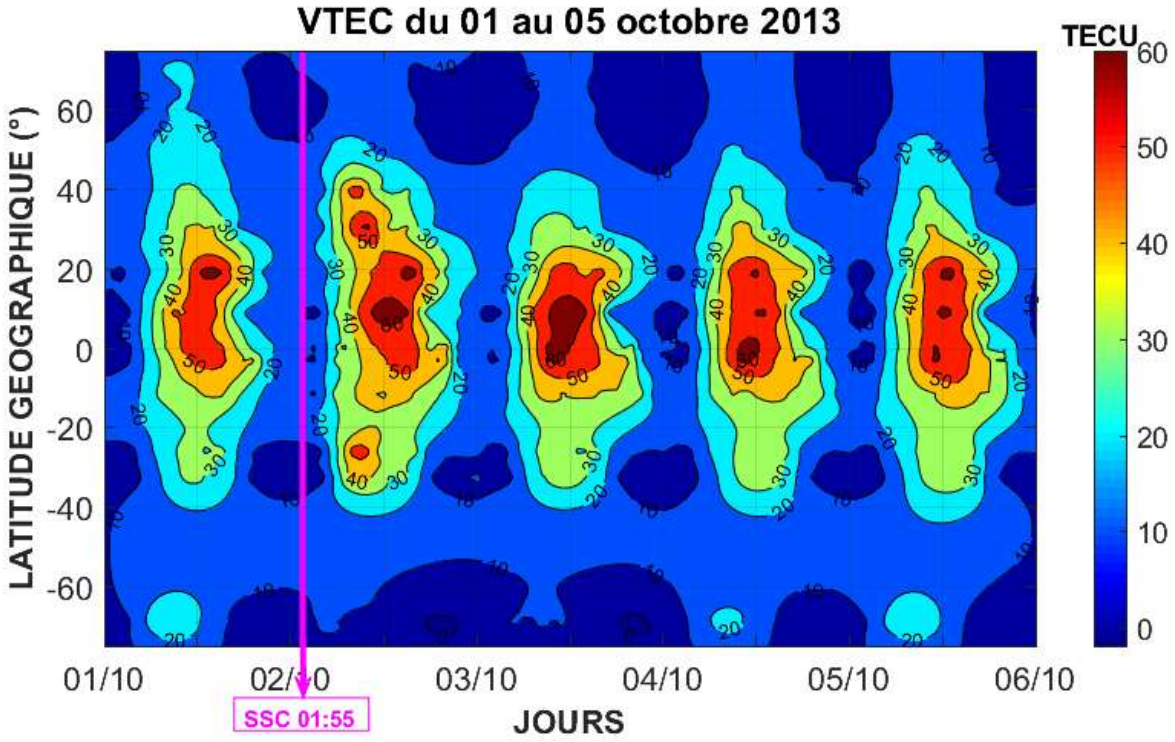

Figure 5b: Latitude–time contour map of vertical total electron content (VTEC) from 01 to 05 October 2013. The color scale (in TECU) illustrates the latitudinal distribution and temporal evolution of ionospheric electron content, with the magenta line indicating the SSC at 01:55 UT.

Figure 5c highlights a pronounced positive ionospheric storm (ΔVTEC > +50%) around 00 UT on 2 October, just before the storm onset at 01:55 UT, localized at northern high latitudes and at the position of the northern EIA crest. After the storm onset, around 08 UT and 16 UT, positive deviations of similar magnitude (ΔVTEC > +50%) are observed at northern mid-latitudes. During the night of 2–3 October, between 22 UT and 01 UT, the deviation becomes positive again at northern high latitudes (ΔVTEC > +100%) as well as at the northern EIA crest (ΔVTEC > +50%). In contrast, at southern high latitudes, strong negative values (ΔVTEC < −50%) are present between 2 and 4 October, as well as around 18 UT on 1, 4, and 5 October. Similar negative ΔVTEC values (ΔVTEC < −50%) are also observed at northern high latitudes around 12 UT on 2 October and around 11 UT on 3 October.

The evolution of TEC deviations, characterized by more pronounced positive values in the Northern Hemisphere and negative values in the Southern Hemisphere, clearly indicates an interhemispheric asymmetry in the ionospheric response to the geomagnetic storm.

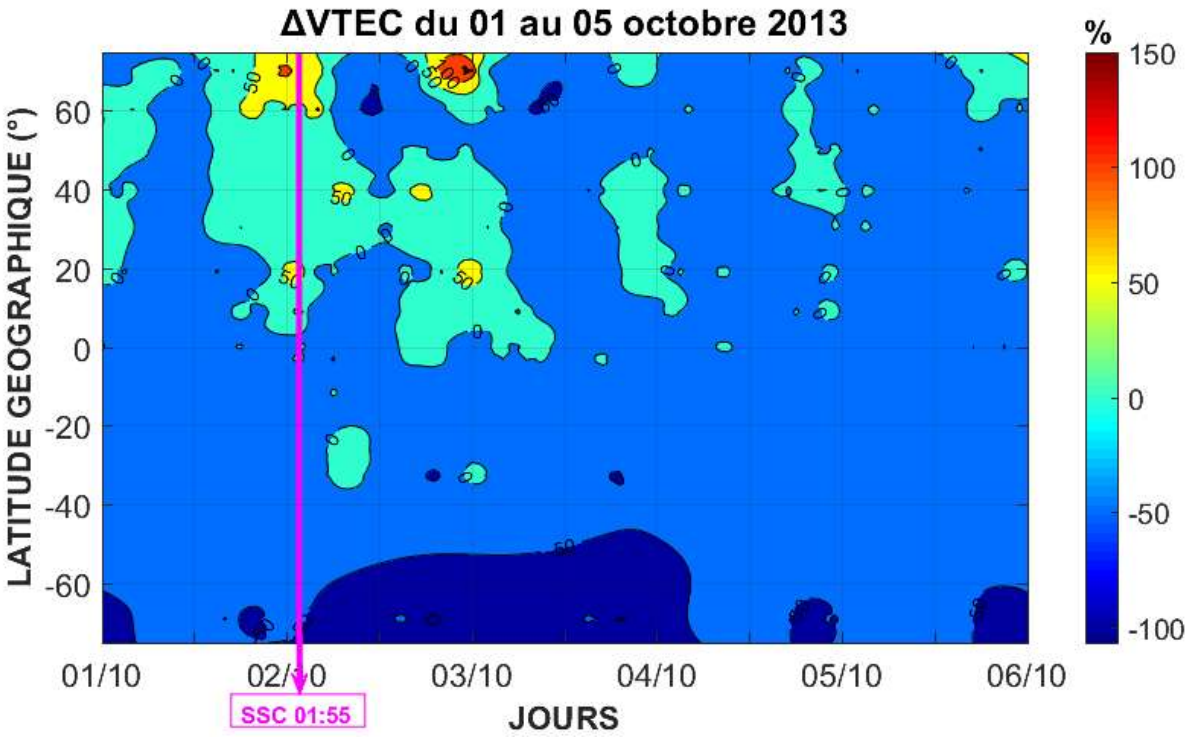

Figure 5c:Latitude–time contour map of relative variations in vertical total electron content (ΔVTEC, %) from 01 to 05 October 2013. The color scale represents percentage deviations from quiet-time conditions. The magenta line marks the Sudden Storm Commencement (SSC) at 01:55 UT.

The storm of February 27, 2014

Figure 6.a illustrates the variations in VTEC between February 26 and March 3, 2014. On February 26 and 27, before the storm began, the maximum VTEC values were already higher than those on calm days for all stations, with increases ranging from +5.7 to +24.3 TECU. The magnetic storm began on February 27 at 16:50 UT. A few hours later, around 23 UT, a sharp increase in VTEC was observed, first at high northern latitudes, then in the equatorial region.

On February 28, most stations still recorded maximum VTEC values higher than those of the calm reference (from +2.3 to +32.9 TECU), with the exception of MZUZ, whose maximum value (78.7 TECU) remained comparable to that of the calm day (77.8 TECU), and SYOG, which showed a notable decrease of –9.1 TECU (29.4 TECU compared to 38.5 TECU in calm conditions). These positive effects are much more pronounced in the northern hemisphere. In low latitudes, there is also a time shift in the VTEC peak, which is reached earlier than on calm days. In contrast, in high latitudes, February 28 is characterized by a decrease in maximum VTEC values compared to February 27.

On March 1, all stations recorded a further significant increase in maximum VTEC values, ranging from +8.3 TECU (SYOG) to +32.5 TECU (NAMA), with a particularly pronounced intensification in the northern hemisphere. On March 2, VTEC remains above the calm reference in the northern hemisphere, while the increase becomes negligible in the southern hemisphere, even negative at high latitudes (SYOG: 35.7 TECU versus 38.5 TECU, or –2.8 TECU). Finally, on March 3, the maximum VTEC values increased again compared to the reference, with the intensity once again stronger in the northern hemisphere (e.g., +28.8 TECU at NAMA compared to +4.2 TECU at SYOG).

Overall, this trend clearly highlights a persistent hemispheric asymmetry in VTEC, which was already present before the magnetic storm began and amplified throughout the storm.

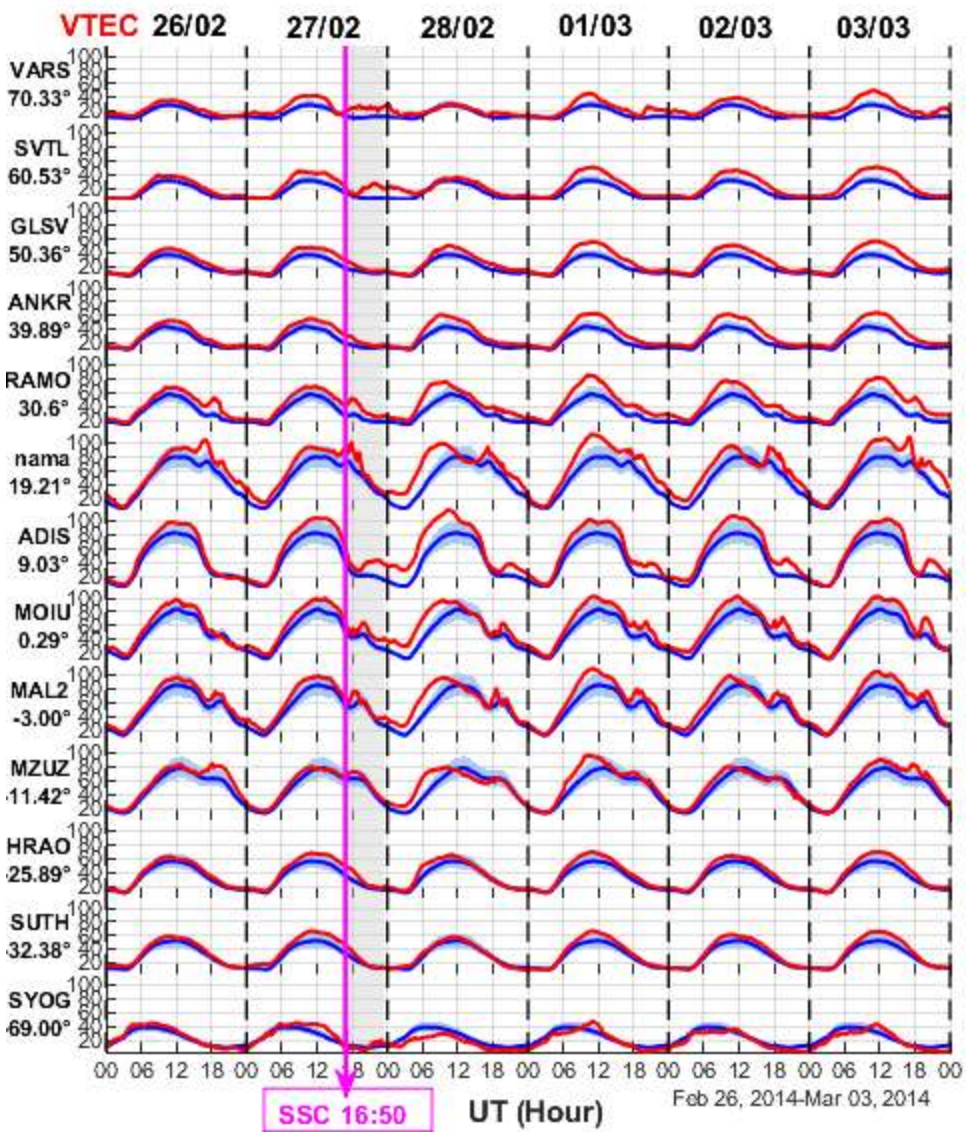

Figure 6.a: Temporal variation of vertical total electron content (VTEC) observed at multiple GNSS stations from February 26 to March 03, 2014. The vertical magenta line marks the SSC at 16:50 UT, highlighting the ionospheric response to the geomagnetic disturbance across different latitudes.

Figure 6.b shows that on February 27, before the storm began, VTEC values were high (around 100 TECU) centered on the magnetic equator, while the peaks of the equatorial ionospheric anomaly (EIA) were absent. On February 28, an intensification of VTEC is observed at the equator, with values exceeding 100 TECU, still accompanied by a disappearance of the peaks. At the same time, a decrease in VTEC is visible at high and mid northern and southern latitudes, compared to February 27 and March 1.

On March 2, the behavior observed on February 27 persisted but was less pronounced. However, March 1 and 3 were notable for the reappearance of the EIA ridges and their marked intensification. A hemispheric asymmetry is also visible, both in intensity and extent. For example, on March 1, the northern ridge of the EIA reaches VTEC values greater than 100 TECU, while the southern ridge has values close to 100 TECU. On March 1 and 3, the southern crest appears narrower than that of the northern hemisphere, confirming this ionospheric asymmetry.

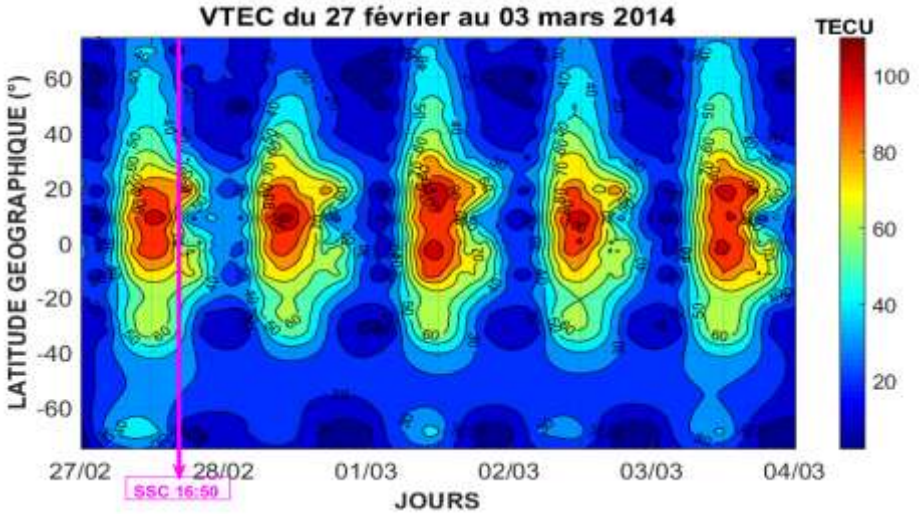

Figure 6.b: Latitude–time contour map of vertical total electron content (VTEC) from February 27 to 03 March 2014. The color scale (in TECU) illustrates the latitudinal distribution and temporal evolution of ionospheric electron content, with the magenta line indicating the SSC at 16:50 UT.

Figure 6.c reveals a marked positive ionospheric storm, with a ΔVTEC of approximately +100% on February 27 at around 01 UT at the position of the northern crest of the EIA. During the night of February 27 to 28, very intense positive variations were observed at high northern latitudes and around the magnetic equator, at around 00 UT and 02 UT respectively, with a ΔVTEC reaching up to +200%. The deviation was already positive at high northern latitudes, with a ΔVTEC of approximately +50% even before the magnetic storm began, then intensified sharply during the magnetic disturbance and spread towards the magnetic equator.

At high northern latitudes, positive deviations with ΔVTEC values between +50% and +100% are visible from February 28 to March 3, except during the day around 12 UT on February 28 and a few hours before 12 UT on March 2. Over the same period, deviations are positive around the magnetic equator, mainly during the night, with ΔVTEC varying between +50% and +100%. In contrast, the deviation is strongly negative (ΔVTEC around –50%) only on March 2, at high southern latitudes, around 22 UT.

All of these changes clearly highlight a hemispheric asymmetry: positive ionospheric disturbances are more pronounced and persistent in the northern hemisphere than in the southern hemisphere.

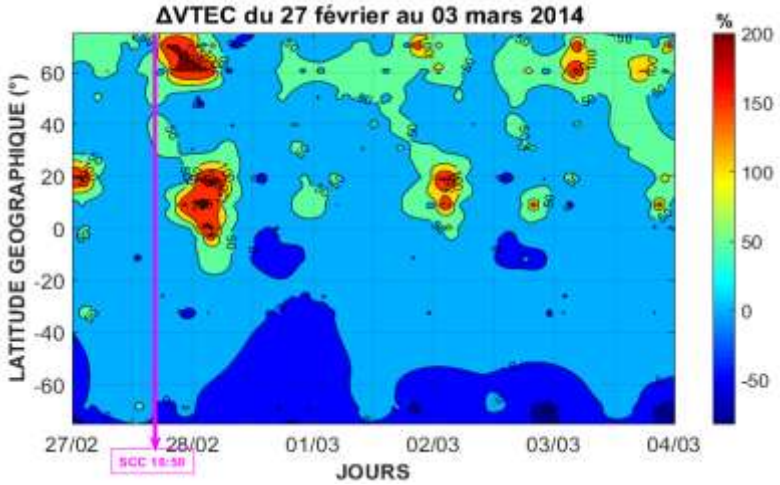

Figure 6.c: Latitude–time contour map of relative variations in vertical total electron content (ΔVTEC, %) from 27 February to 03 March 2014. The color scale represents percentage deviations from quiet-time conditions. The magenta line marks the Sudden Storm Commencement (SSC) at 16:50 UT.

Satellite Data

Figures 7a–7d present the global variations of the thermospheric O/N_2 ratio derived from observations by the Global Ultraviolet Imager (GUVI) onboard the TIMED satellite during the geomagnetic storms of 13–18 July 2012, 15–20 March 2013, 30 September–5 October 2013, and 26 February–3 March 2014.

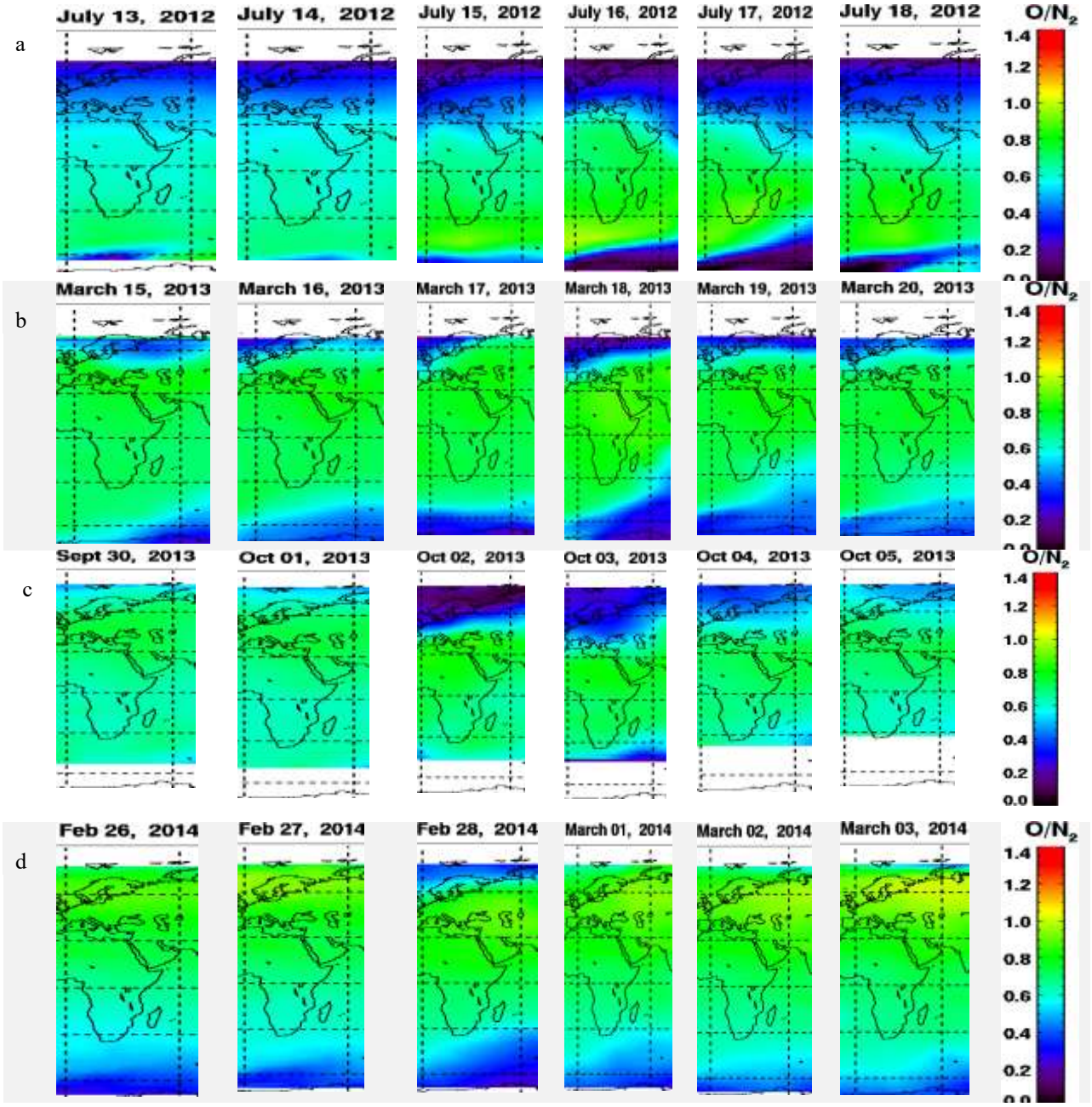

Figure 7 (a–d):Thermospheric O/N_2 ratio derived from GUVI/TIMED observations during the geomagnetic storms of 13–18 July 2012, 15–20 March 2013, 30 September–5 October 2013, and 26 February–3 March 2014.

Analysis of GUVI-derived O/N_2 maps at the GNSS station locations reveals, for each storm, a pronounced depletion at high latitudes followed by a gradual equatorward migration toward mid-latitudes, with no significant modification at low latitudes. For the 14 July 2012 storm (13–18 July), the initial high-latitude depletion progressively extended

toward mid-latitudes. During the 17 March 2013 storm (15–20 March), the depletion detected at high latitudes migrated toward Southern Hemisphere mid-latitudes on 18 and 19 March. During the 2 October 2013 storm (2–4 October), the O/N_2 reduction initially concentrated at high latitudes propagated toward mid-latitudes on 2 and 3 October. Finally, for the 27 February 2014 storm (26 February–3 March), a significant reduction was observed as early as 26 February at southern high latitudes before extending toward mid-latitudes, whereas in the Northern Hemisphere it was detected only on 28 February.

Discussion:-

Based on data from a network of GPS receivers distributed in latitude across both hemispheres in the Europe–Africa–Antarctica sector (longitudes 20°E–40°E), and by combining a station-by-station analysis with panel superposition and the use of regional VTEC and ΔVTEC maps, we highlighted contrasting ionospheric responses during geomagnetic storms.

The positive, and sometimes negative, variations observed during days classified as magnetically quiet prior to storm onset can be explained by the fact that these days were not entirely free of magnetic disturbances. Thus, for the 17 March 2013 storm, the increase in VTEC recorded on 16 March (reference day) can be attributed to the substorm that occurred around 05 UT, as evidenced by the AE index reaching 863 nT at 04:49 UT. Wei et al. (2009) indeed showed that substorms can induce such increases in VTEC at equatorial latitudes. Previous studies (Kane 1973; Araujo-Pradere et al. 2002; Burešová et Laštovička 2007) reported a pre-storm effect on foF2 about 24 h before the SSC, although this interpretation has been debated (Mikhailov et Perrone 2009). Burešová and Laštovička (2007) , in a study of 65 major storms between 1995 and 2005, showed that 20–25% of them exhibited a pronounced pre-storm effect.

The increase observed prior to the 14 July 2012 storm is consistent with the observations of Tesema et al. (2015), who reported an enhancement of TEC at the equator and northern mid-latitudes, accompanied by a decrease at the EIA crests in both hemispheres. In our case, only the positive effect is remarkable, localized at the transition between low and mid-latitudes. This may be related to the choice of reference, since Tesema et al. (2015) considered only the single quietest day as reference. For the 17 March 2013 storm, Zhu et al. (2022) and Yue et al. (2016) included 16 March in the reference period, which explains the absence of pre-storm anomalies in their results.

The persistent negative responses observed at mid and high latitudes during these four storms are mainly explained by a strong depletion of the O/N_2 ratio, as illustrated in Figures 7(a–c). There is indeed a close correlation between electron density and neutral composition variations during storms (Liu et al. 2014). A reduction in atomic oxygen decreases ion production, while an increase in molecular nitrogen enhances ionization losses, leading to a net decrease in electron density (Prölss 1995). Joule heating at high latitudes during storms increases temperature and drives upward winds that transport N_2-rich and O-poor air from the lower thermosphere into the F region (Fuller-Rowell et al. 1994; Qian, Burns, et al. 2014). This process induces a strong horizontal pressure gradient and equatorward neutral winds, causing the O/N_2 deficit to propagate toward mid and low latitudes (Kil et al. 2013; Meier et al. 2015). In parallel, downward motion of O-rich and N_2-poor air at lower latitudes leads to a local increase in the O/N_2 ratio, which can subsequently propagate toward the equator through horizontal transport (Immel et al. 2001; Cai et al. 2022).

For the 14 July 2012 storm, the mechanisms responsible for ionospheric asymmetry have been extensively described by Tesema et al. (2015) and Liu et al. (2014). After the SSC (14 July at 18:09 UT), a strong decrease in VTEC appears around 22 UT at stations close to the magnetic equator (NAMA, ADIS, MOIU), while a slight increase is observed at the EIA crests (RAMO, MZUZ). This can be attributed to an equatorward neutral wind, as suggested by the high AE values (1772 nT at 18:48 UT), indicative of significant energy deposition at high latitudes. Such a neutral wind can transport plasma to higher latitudes more efficiently than the super-fountain effect (Liu et al. 2014). The action of an eastward PPEF prior to its reversal westward, followed by redistribution, is also possible. Around 19 UT, the interplanetary Bz component oscillated with longer intervals southward than northward and with pressure exceeding 5 nPa, conditions favorable for the generation of a PPEF capable of affecting the E×B drift.
On 15 July, the marked strengthening of the EIA can also be attributed to an eastward PPEF. Before 12 UT, Bz remained southward and the pressure exceeded 20 nPa, again providing favorable conditions for a penetrating electric field. Liu et al. (2014) indeed identified several PPEFs during this event. The decrease observed near the magnetic equator, while other stations showed intensification, confirms this scenario (Liu et al. 2014). The

persistence of a pronounced positive phase at northern mid-latitudes around 12 UT may instead be attributed to an enhancement of the equatorial anomaly (Tesema et al. 2015).

The contrasting responses recorded between 15 and 16 July are explained by changes in thermospheric composition and the action of storm-induced neutral winds (Tesema et al. 2015; Stankov et al. 2010). Overall, our results confirm previous observations (Akala et al. 2012; Chakraborty et al. 2015; Azzouzi 2016; Tesema et al. 2015), namely a positive TEC response at equatorial low latitudes and a negative response at mid and high latitudes during the 14 July 2012 storm.

2013 storm, the inhibition of the EIA, the amplification of the positive response at mid-latitudes, and the observed interhemispheric asymmetry are consistent with the results of Yue et al. (2016), obtained from satellite, ground-based, and theoretical modeling data. These phenomena can be explained by the combined action of polar meridional winds and perturbations of the E×B drift. Liu et al. (2014) further emphasize that neutral winds play a dominant role in generating vertical ion drifts at mid-latitudes, to the detriment of PPEF effects. The interhemispheric asymmetry may be due to the presence of TADs, as indicated by VTEC oscillations and high AE values (>2500 nT). During equinox periods, electric field and neutral wind effects alone are insufficient to explain this asymmetry, with O/N_2 depletion being more decisive. (Prölss 1995; Zhu et al. 2022; Yue et al. 2016) also showed that TADs can generate such asymmetries in the EIA region during the afternoon. Finally, Migoya-Orue et al. (2021) reported an increase in VTEC over the northern EIA crest in Africa, consistent with our results.

During the 2 October storm, the depletion of the O/N_2 ratio (Figure 7c) correlates well with the negative responses observed at high latitudes. However, it is insufficient to explain the persistent disturbances observed at mid-latitudes after the positive phase. These are likely the result of the combined action of O/N_2 depletion and a westward DDEF. The positive disturbances at mid-latitudes and the VTEC oscillations may be related to an eastward PPEF, reinforced by neutral wind action and the presence of TADs. The southward excursion of Bz (−28.8 nT at 04:58 UT) and the strong dynamic pressure (53.17 nPa at 05:25 UT) make the occurrence of a PPEF plausible. Disturbances migrating from high latitudes, associated with high AE values (2089 nT) and VTEC oscillations, are characteristic of TADs (Fuller-Rowell et al. 1994 ; Pandit et al. 2023). The inhibition of the EIA and the amplification of the positive response at mid-latitudes agree with the scenarios proposed by (Yue et al. 2016; Liu et al. 2014). Finally, the difference in the intensity of positive responses between hemispheres can be explained by asymmetric TAD phase velocities related to Joule heating deposition (Zhu et al. 2022).

For the 27 February 2014 storm, the high VTEC values recorded prior to onset are consistent with the results of (Malki et al. 2018) at Rabat. Accounting for the time shift, the increase observed around 23 UT on 27 February is also consistent with these studies and is attributed to plasma transport by TADs. The negative responses at high latitudes are correlated with the depletion of the O/N_2 ratio (Figure 7d). The pronounced VTEC increases observed on 1 and 3 March are likely associated with substorms, as suggested by the strong AE enhancements concomitant with decreases in the SYM/H index during these days. Wei et al. (2009) had already shown that such phenomena can increase equatorial VTEC. Finally, the asymmetries observed from the initial phase are consistent with previous observations reporting positive responses in the winter hemisphere and negative responses in the summer hemisphere (Fuller-Rowell et al. 1994).

(Shimeis et al. 2015) analyzed TEC variations along a latitudinal chain of GPS stations between 20°E and 40°E, spanning from northern high latitudes to southern high latitudes. Their study revealed strong interhemispheric asymmetry as well as a TID propagating from high to low latitudes. The authors explained that this asymmetry, observed at equinox, results from several concurrent mechanisms, including solar activity, atmospheric dynamo effects, and the offset between geographic and geomagnetic axes.

Conclusions:-

In this article, we presented an analysis of the ionospheric response during four major geomagnetic storms that occurred between 2012 and 2014, based on data from several GNSS receivers located at low, mid, and high latitudes along a longitude axis between 20° and 40° East.

The results show, first of all, that high and mid-latitudes are dominated by persistent negative deviations. These can be explained largely by changes in thermospheric composition during storms, in particular the decrease in the O/N_2 ratio, which significantly reduces electron density and contributes directly to the decrease in VTEC. At mid-

latitudes, the ionospheric response is more nuanced, marked by alternating positive and negative effects. This variability reflects the combined action of the electric penetration field and neutral circulation. At low latitudes, the dynamics of the equatorial ionospheric anomaly (EIA) showed notable changes, with an intensification during phases dominated by the PPEF, and a suppression under the effect of disturbed neutral winds.
Finally, a marked interhemispheric asymmetry was observed, confirming the influence of ionospheric seasonality and TADs on the differential evolution of VTEC between the two hemispheres during a magnetic storm.

Conflict of interest
The authors have declared no conflicts of interest

Acknowledgements:-

The authors would like to thank the institutions and services that provided the data used in this study. The RINEX data files from the various stations were obtained from the UNAVCO website (http://www.unavco.org).The time series data for solar wind and interplanetary magnetic field parameters (Vsw, Psw, Bz), as well as the AE and SYM/H geomagnetic indices, with a resolution of one minute, were obtained from the OMNI database (https://omniweb.gsfc.nasa.gov/form/omni_min.html).The Kp and Dst indices, as well as the dates of sudden storm commencements (SSCs), are available via the ISGI service (https://isgi.unistra.fr/data_download.php).Finally, the [O/N_2] ratio maps, derived from the Global Ultraviolet Imager (GUVI) aboard the TIMED satellite, were used to interpret the results and are available via the portal https://guvitimed.jhuapl.edu/guvi-galleryl3on2_new/.

References:-

1. Akala, A. O., P. H. Doherty, C. S. Carrano, C. E. Valladares, et K. M. Groves. 2012. « Impacts of ionospheric scintillations on GPS receivers intended for equatorial aviation applications ». Radio Science 47 (04): 1-11.
2. Akala, A.O., A.B. Rabiu, E.O. Somoye, E.O. Oyeyemi, et A.B. Adeloye. 2013. « The Response of African Equatorial GPS-TEC to Intense Geomagnetic Storms during the Ascending Phase of Solar Cycle 24 ». Journal of Atmospheric and Solar-Terrestrial Physics 98 (juin): 50-62. https://doi.org/10.1016/j.jastp.2013.02.006.
3. Alenazi, Moqbil Salem, Hassan Mahdy Nooreldeen, Ayman Mahmoud Ahmed, et al. 2025. « Investigation of Ionospheric Response to a Moderate Geomagnetic Storm over the Mid-Latitude of Saudi Arabia ». Open Astronomy 34 (1): 20240009. https://doi.org/10.1515/astro-2024-0009.
4. Araujo-Pradere, E. A., T. J. Fuller-Rowell, et M. V. Codrescu. 2002. « STORM: An empirical storm-time ionospheric correction model: 1. Model description ». Radio Science 37 (5): 1-12.
5. Astafyeva, E. 2009. « Effects of Strong IMF B_Z Southward Events on the Equatorial and Mid-Latitude Ionosphere ». Annales Geophysicae 27 (3): 1175-87. https://doi.org/10.5194/angeo-27-1175-2009.
6. Atıcı, Ramazan, et SelçukSağır. 2020. « Global Investigation of the Ionospheric Irregularities during the Severe Geomagnetic Storm on September 7–8, 2017 ». Geodesy and Geodynamics 11 (3): 211-21. https://doi.org/10.1016/j.geog.2019.05.004.
7. Azzouzi, Ilyasse. 2016. « Impact des evènements solaires sur l'ionisation de l'ionosphère des moyennes et basses latitudes dans le secteur Europe-Afrique ». Universite Pierre et Marie Curie- Paris VI; PhD Thesis, Universite Mohammed V.
8. Balan, N., K. Shiokawa, Y. Otsuka, et al. 2010. « A physical mechanism of positive ionospheric storms at low latitudes and midlatitudes ». Journal of Geophysical Research: Space Physics 115 (A2).
9. Bazie, Nongobsom, Christian Zoundi, M'BI Kabore, Alfred Jean Stephane Dama, et Frederic Ouattara. 2025. « Response of the magnetospheric convection electric field (MCEF) to geomagnetic storms during the solar cycle 24 declining phase ». Journal of the Nigerian Society of Physical Sciences, 2696-2696.
10. Berenyi, K. A., B. Heilig, J. Urbář, D. Kouba, Á. Kis, et V. Barta. 2023. « Comprehensive Analysis of the Ionospheric Response to the Largest Geomagnetic Storms from Solar Cycle 24 over Europe ». Frontiers in Astronomy and Space Sciences 10 (avril): 1092850. https://doi.org/10.3389/fspas.2023.1092850.
11. Blanch, E., S. Marsal, A. Segarra, J. M. Torta, D. Altadill, et J. J. Curto. 2013. « Space Weather Effects on Earth's Environment Associated to the 24–25 October 2011 Geomagnetic Storm ». Space Weather 11 (4): 153-68. https://doi.org/10.1002/swe.20035.
12. Buonsanto, M. Ji. 1999. « Ionospheric storms—a review ». Space Science Reviews 88 (3): 563-601.
13. Burešová, D[illegible], et J. Laštovička. 2007. « Pre-storm enhancements of foF2 above Europe ». Advances in Space Research 39 (8): 1298-303.

14. Cai, Xuguang, Wenbin Wang, Alan Burns, Liying Qian, et Richard W. Eastes. 2022. « The Effects of IMF B_y on the Middle Thermosphere During a Geomagnetically "Quiet" Period at Solar Minimum ». Journal of Geophysical Research: Space Physics 127 (5): e2021JA029816. https://doi.org/10.1029/2021JA029816.
15. Chakraborty, Monti, Sanjay Kumar, Barin Kumar De, et Anirban Guha. 2015. « Effects of Geomagnetic Storm on Low Latitude Ionospheric Total Electron Content: A Case Study from Indian Sector ». Journal of Earth System Science 124 (5): 1115-26. https://doi.org/10.1007/s12040-015-0588-3.
16. Curto, J. J., S. Marsal, E. Blanch, et D. Altadill. 2018. « Analysis of the Solar Flare Effects of 6 September 2017 in the Ionosphere and in the Earth's Magnetic Field Using Spherical Elementary Current Systems ». Space Weather 16 (11): 1709-20. https://doi.org/10.1029/2018SW001927.
17. Davies, Kenneth. 1990. Ionospheric radio. n° 31. Iet.
18. Fuller-Rowell, T. J., M. V. Codrescu, R. J. Moffett, et S. Quegan. 1994. « Response of the Thermosphere and Ionosphere to Geomagnetic Storms ». Journal of Geophysical Research: Space Physics 99 (A3): 3893-914. https://doi.org/10.1029/93JA02015.
19. Fuller-Rowell, Tim, Mihail Codrescu, Naomi Maruyama, et al. 2007. « Observed and modeled thermosphere and ionosphere response to superstorms ». Radio science 42 (04): 1-9.
20. Gao, Jay. 2008. Digital analysis of remotely sensed imagery. McGraw-Hill Professional.
21. Gonzalez, W. D., Jo-Ann Joselyn, Yohsuke Kamide, et al. 1994. « What is a geomagnetic storm? » Journal of Geophysical Research: Space Physics 99 (A4): 5771-92.
22. Habyarimana, Valence. 2023. Jean Bosco Habarulema2 et Teshome Dugassa3.
23. Hunsucker, Robert D., et John Keith Hargreaves. 2007. The high-latitude ionosphere and its effects on radio propagation. Cambridge University Press.
24. Immel, T. J., et A. J. Mannucci. 2013. « Ionospheric redistribution during geomagnetic storms ». Journal of Geophysical Research: Space Physics 118 (12): 7928-39.
25. Immel, Thomas J., Geoff Crowley, John D. Craven, et Raymond G. Roble. 2001. « Dayside enhancements of thermospheric O/N2 following magnetic storm onset ». Journal of Geophysical Research: Space Physics 106 (A8): 15471-88.
26. Kane, R. P. 1973. « Global evolution of F2-region storms ». Journal of Atmospheric and Terrestrial Physics 35 (11): 1953-66.
27. Kelley, Michael C. 2009. The Earth's ionosphere: Plasma physics and electrodynamics. Vol. 96. Academic press.
28. Kil, H., W. K. Lee, J. Shim, L. J. Paxton, et Y. Zhang. 2013. « The Effect of the 135.6 Nm Emission Originated from the Ionosphere on the TIMED/GUVI O/N_2 Ratio ». Journal of Geophysical Research: Space Physics 118 (2): 859-65. https://doi.org/10.1029/2012JA018112.
29. Kuai, Jiawei, Libo Liu, Jing Liu, et al. 2016. « Effects of Disturbed Electric Fields in the Low-latitude and Equatorial Ionosphere during the 2015 St. Patrick's Day Storm ». Journal of Geophysical Research: Space Physics 121 (9): 9111-26. https://doi.org/10.1002/2016JA022832.
30. Liu, Jing, Libo Liu, Takuji Nakamura, Biqiang Zhao, Baiqi Ning, et A. Yoshikawa. 2014. « A Case Study of Ionospheric Storm Effects during Long-lasting Southward IMF B_z -driven Geomagnetic Storm ». Journal of Geophysical Research: Space Physics 119 (9): 7716-31. https://doi.org/10.1002/2014JA020273.
31. Liu, Yi Y., Richard AM De Jeu, Matthew F. McCabe, Jason P. Evans, et Albert IJM Van Dijk. 2011. « Global long-term passive microwave satellite-based retrievals of vegetation optical depth ». Geophysical Research Letters 38 (18).
32. Malki, Khalifa, Aziza Bounhir, Zouhair Benkhaldoun, et al. 2018. « Ionospheric and Thermospheric Response to the 27–28 February 2014 Geomagnetic Storm over North Africa ». Annales Geophysicae 36 (4): 987-98. https://doi.org/10.5194/angeo-36-987-2018.
33. Mao, Tian, Lingfeng Sun, Lianhuan Hu, Yungang Wang, et Zhijun Wang. 2015. « A Case Study of Ionospheric Storm Effects in the Chinese Sector during the October 2013 Geomagnetic Storm ». Advances in Space Research 56 (9): 2030-39. https://doi.org/10.1016/j.asr.2015.05.045.
34. Matamba, Tshimangadzo Merline, John Bosco Habarulema, et Lee-Anne McKinnell. 2015. « Statistical analysis of the ionospheric response during geomagnetic storm conditions over South Africa using ionosonde and GPS data ». Space Weather 13 (9): 536-47.
35. Meier, R. R., J. M. Picone, D. Drob, et al. 2015. « Remote Sensing of Earth's Limb by TIMED/GUVI: Retrieval of Thermospheric Composition and Temperature ». Earth and Space Science 2 (1): 1-37. https://doi.org/10.1002/2014EA000035.
36. Mendillo, M., et C. Narvaez. 2009. « Ionospheric storms at geophysically-equivalent sites–Part 1: Storm-time patterns for sub-auroral ionospheres ». Annales Geophysicae 27 (4): 1679-94.

37. Mendillo, M., et C. Narvaez. 2010. « Ionospheric storms at geophysically-equivalent sites–Part 2: Local time storm patterns for sub-auroral ionospheres ». Annales Geophysicae 28 (7): 1449-62.
38. Mendillo, Michael. 2006. « Storms in the ionosphere: Patterns and processes for total electron content ». Reviews of Geophysics 44 (4).
39. Migoya-Orue, Y. O., S. M. Radicella, et P. Coïsson. 2009. « Low latitude ionospheric effects of major geomagnetic storms observed using TOPEX TEC data ». Annales geophysicae 27 (8): 3133-39.
40. Migoya-Orue, Yenca, Katy Alazo-Cuartas, Anton Kashcheyev, et al. 2021. « B2 Thickness Parameter Response to Equinoctial Geomagnetic Storms ». Sensors 21 (21): 7369. https://doi.org/10.3390/s21217369.
41. Mikhailov, A. V̂, et L. Perrone. 2009. « Pre-storm NmF2 enhancements at middle latitudes: delusion or reality ? » Annales Geophysicae 27 (3): 1321-30.
42. Omojola, Joseph, et Taiwo Adewumi. 2019. « Effects of St Patrick's Day Intervals Geomagnetic Storms on the Accuracy of GNSS Positioning and Total Electron Content over Nigeria ». يزيد كزم ين فـ ضا و ف, n° Online First (janvier). https://doi.org/10.22059/jesphys.2019.259772.1007014.
43. Ouattara, Frederic, Christian Zoundi, Christine Amory MAZAUDIER, Rolland FLEURY, et Patrick LASSUDRIE DUCHESNE. 2011. « Determination du contenu electronique total à partir des pseudo distances (Pd) ou pseudo range (Pr) a la station de Koudougou au Burkina Faso ». Journal des Sciences11: 12-19.
44. Ouedraogo, Pouraogo, Karim Guibula, Abidina Diabate, Rolland Fleury, et Frederic Ouattara. 2024. « Study of Regular Variations in Vertical Total Electron Content (VTEC) from 2013 to 2021 at Station BF01 in Ouagadougou ». Current Journal of Applied Science and Technology 43 (7): 103-17. https://doi.org/10.9734/cjast/2024/v43i74410.
45. Pandit, D., C. Amory-Mazaudier, R. Fleury, N. P. Chapagain, et B. Adhikari. 2023. « VTEC Observations of Intense Geomagnetic Storms above Nepal: Comparison with Satellite Data, CODE and IGSG Models ». Indian Journal of Physics 97 (3): 701-18. https://doi.org/10.1007/s12648-022-02441-w.
46. Pedatella, Nicholas M., Jiuhou Lei, Kristine M. Larson, et Jeffrey M. Forbes. 2009. « Observations of the ionospheric response to the 15 December 2006 geomagnetic storm: Long-duration positive storm effect ». Journal of Geophysical Research: Space Physics 114 (A12).
47. Prölss, G. W. 1995. Handbook of Atmospheric Electrodynamics, Volume IIHandbook of Atmospheric. CRC Press.
48. Pulkkinen, Tuija. 2007. « Space Weather: Terrestrial Perspective ». Living Reviews in Solar Physics 4. https://doi.org/10.12942/lrsp-2007-1.
49. Qian, Liying, Alan G Burns, Barbara A Emery, et al. 2014. « The NCAR TIE-GCM: A community model of the coupled thermosphere/ionosphere system ». Modeling the ionosphere–thermosphere system, 73-83.
50. Qian, Liying, Stanley C. Solomon, et Raymond G. Roble. 2014. « Secular changes in the thermosphere and ionosphere between two quiet Sun periods ». Journal of Geophysical Research: Space Physics 119 (3): 2255-62.
51. Richmond, A. D., et G. Lu. 2000. « Upper-atmospheric effects of magnetic storms: a brief tutorial ». Journal of Atmospheric and Solar-Terrestrial Physics 62 (12): 1115-27.
52. Rishbeth, H., et I. C. F. Müller-Wodarg. 2006. « Why is there more ionosphere in January than in July? The annual asymmetry in the F2-layer ». Annales Geophysicae 24 (12): 3293-311.
53. Sawadogo, Saguedo, Doua Allain Gnabahou, Sibri Alphonse Sandwidi, et Frederic Ouattara. 2023. « Koudougou (Burkina Faso, Africa), GPS-TEC Response to Recurrent Geomagnetic Storms during Solar Cycle 24 Declining Phase ». International Journal of Geophysics 2023 (avril): 1-13. https://doi.org/10.1155/2023/4181389.
54. Sharma, Sunil Kumar, Arun Kumar Singh, Sampad Kumar Panda, et Sameh S. Ahmed. 2020. « The Effect of Geomagnetic Storms on the Total Electron Content over the Low Latitude Saudi Arab Region: A Focus on St. Patrick's Day Storm ». Astrophysics and Space Science 365 (2): 35. https://doi.org/10.1007/s10509-020-3747-1.
55. Shimeis, A., C. Borries, C. Amory-Mazaudier, et al. 2015. « TEC Variations along an East Euro-African Chain during 5th April 2010 Geomagnetic Storm ». Advances in Space Research 55 (9): 2239-47. https://doi.org/10.1016/j.asr.2015.01.005.
56. Shreedevi, P. R., et R. K. Choudhary. 2017. « Impact of Oscillating IMF B_z During 17 March 2013 Storm on the Distribution of Plasma Over Indian Low-Latitude and Mid-Latitude Ionospheric Regions ». Journal of Geophysical Research: Space Physics 122 (11). https://doi.org/10.1002/2017JA023980.
57. Silwal, Ashok, Sujan Prasad Gautam, Prakash Poudel, Monika Karki, Narayan P Chapagain, et Binod Adhikari. 2023. « Variation of Total Electron Content over Nepal during Geomagnetic Storms: GPS Observations ». Russian Journal of Earth Sciences, août 13, 1-19. https://doi.org/10.2205/2023ES000833.

58. Stankov, S. M., Koen Stegen, et Rene Warnant. 2010. « Seasonal variations of storm-time TEC at European middle latitudes ». Advances in Space Research 46 (10): 1318-25.
59. Tesema, F., B. Damtie, et M. Nigussie. 2015. « The Response of the Ionosphere to Intense Geomagnetic Storms in 2012 Using GPS-TEC Data from East Africa Longitudinal Sector ». Journal of Atmospheric and Solar-Terrestrial Physics 135 (decembre) : 143-51. https://doi.org/10.1016/j.jastp.2015.10.021.
60. Tsurutani, Bruce T., Walter D. Gonzalez, et Yohsuke Kamide. 1997. « Magnetic storms ». Surveys in geophysics 18 (4): 363-83.
61. Uga, Chali Idosa, Sujan Prasad Gautam, et Ephrem Beshir Seba. 2024. « TEC Disturbances Caused by CME-Triggered Geomagnetic Storm of September 6–9, 2017 ». Heliyon 10 (10): e30725. https://doi.org/10.1016/j.heliyon.2024.e30725.
62. Vijaya Lekshmi, D., N. Balan, S. Tulasi Ram, et J. Y. Liu. 2011. « Statistics of Geomagnetic Storms and Ionospheric Storms at Low and Mid Latitudes in Two Solar Cycles : GEOMAGNETIC AND IONOSPHERIC STORMS ». Journal of Geophysical Research: Space Physics 116 (A11): n/a-n/a. https://doi.org/10.1029/2011JA017042.
63. Wei, Y., Z. Pu, M. Hong, et al. 2009. « Westward ionospheric electric field perturbations on the dayside associated with substorm processes ». Journal of Geophysical Research: Space Physics 114 (A12).
64. Yu, Tingting, Wenbin Wang, Zhipeng Ren, Xuguang Cai, et Maosheng He. 2023. « Vertical Variations in Thermospheric O/N_2 and the Relationship Between O and N_2 Perturbations During a Geomagnetic Storm ». Earth and Space Science 10 (10): e2023EA002988. https://doi.org/10.1029/2023EA002988.
65. Yue, Xinan, William S. Schreiner, Nicholas Pedatella, et al. 2014. « Space weather observations by GNSS radio occultation : From FORMOSAT-3/COSMIC to FORMOSAT-7/COSMIC-2 ». Space Weather 12 (11): 616-21.
66. Yue, Xinan, Wenbin Wang, Jiuhou Lei, et al. 2016. « Long-lasting Negative Ionospheric Storm Effects in Low and Middle Latitudes during the Recovery Phase of the 17 March 2013 Geomagnetic Storm ». Journal of Geophysical Research: Space Physics 121 (9): 9234-49. https://doi.org/10.1002/2016JA022984.
67. Zhu, Qingyu, Gang Lu, et Yue Deng. 2022. « Low- and Mid-Latitude Ionospheric Response to the 2013 St. Patrick's Day Geomagnetic Storm in the American Sector: Global Ionosphere Thermosphere Model Simulation ». Frontiers in Astronomy and Space Sciences 9 (mai): 916739. https://doi.org/10.3389/fspas.2022.916739.
68. Zoundi, c., et f. Ouattara. S. D. Processus de determination du contenu electronique total (cet) process for determining total electron content (TEC).